

A local model of snow-firn dynamics and application to Colle Gnifetti site

Fabiola Banfi¹ and Carlo De Michele¹

¹Department of Civil and Environmental Engineering, Politecnico di Milano, Milano, Italy

Correspondence: Fabiola Banfi (fabiola.banfi@polimi.it), Carlo De Michele (carlo.demichela@polimi.it)

Abstract. The regulating role of glaciers on catchment run-off is of fundamental importance in sustaining people living in low lying areas. The reduction in glacierized areas under the effect of climate change disrupts the distribution and amount of run-off, threatening water supply, agriculture and hydropower. The prediction of these changes requires models that integrate hydrological, nivological and glaciological processes. In this work we propose a local model that combines the nivological and glaciological scales. The model describes the formation and evolution of the snowpack and the firn below it, under the influence of temperature, wind speed and precipitation. The model has been implemented in two versions: (1) a multi-layer one that considers separately each firn layer, and (2) a single-layer one that models firn and underlying glacier ice as a single layer. The model was applied at the site of Colle Gnifetti (Monte Rosa massif, 4400–4550 m a.s.l.). We obtained an average reduction of annual snow accumulation due to wind erosion of $2 \cdot 10^3 \text{ kg m}^{-2} \text{ y}^{-1}$ to be compared with a mean annual precipitation of about $2.7 \cdot 10^3 \text{ kg m}^{-2} \text{ y}^{-1}$. The conserved accumulation is made up mainly of snow deposited between April and September, when temperatures above melting point are also observed. End of year snow density, instead, increased in average of 65 kg m^{-3} when the contribution of wind to snow compaction was added. Observations show a high spatial and interannual variability in the characteristics of snow and firn at the site and a correlation of net balance with radiation and number of melt layers. The computation of snowmelt in the model as a solely function of air temperature may therefore be one of the reasons of the observed mismatch between model and observations.

1 Introduction

Glacier ice covers almost 16 million km^2 of the Earth's surface, of which it is estimated that only 3% is retained by the mountains outside the polar regions (Benn and Evans, 2010). Despite this small percentage, the amount of water stored in mountain glaciers plays a key role in sustaining people living in low lying areas (Adhikary, 1993), influencing run-off on a wide range of temporal and spatial scales (Jansson et al., 2003; Huss et al., 2010). Storing water coming from precipitation in winter and delaying the time in which it reaches the river network, they sustain streamflow in hotter and drier periods when precipitation is lacking and when it is most needed for agriculture and as drinking water (Fountain and Tangborn, 1985; Hagg et al., 2007).

Jost et al. (2012) studied a Canadian river basin, covered for only 5% by glaciers, and they found that ice melt contributes up to 25% to streamflow in August, up to 35% to streamflow in September and between 3% and 9% to total streamflow.

In high mountain river basins of the northern Tien Shan (Central Asia), with areas of glaciation higher than 30–40 %, glacier melt contribution is 18–28 % of annual run-off but it can increase to 40–70 % during summer (Aizen et al., 1996).

The reduction of glacier volume observed over the past 150 years (Vaughan et al., 2013; Hock et al., 2019) will result in a change in the present distribution and amount of water storage and release, with implications in all aspects of watershed management (Hock et al., 2005) and with consequent high economic impacts (Huss et al., 2010). The prediction of these changes is therefore fundamental in order to assess and reduce their impacts, optimizing consequently the management of water resources. To accomplish this task, models that integrate hydrological, nivological and glaciological components and that consider a variable glacier extension and the transient response of glacier to climate change are required (Luo et al., 2013).

Despite their importance, fully integrated glacio-hydrological catchment models are not common in literature (Wortmann et al., 2019). Some examples of glacio-hydrological models are provided by the works of Huss et al. (2010); Naz et al. (2014); Seibert et al. (2018) and Wortmann et al. (2019).

Wortmann et al. (2019) grouped the main problems of glacio-hydrological models in two categories: integration and scale. With integration problems they refer to the simplified or absent description of the remaining catchment hydrology in models that describe in detail glacier processes. The decrease in the fraction of ice covered areas requires a proper description of both components, even in basins that are currently highly glaciated. Another aspect is the integration of nivological and glaciological components: a joint simulation of glacier mass balance and snow accumulation and melt is required in order to avoid inconsistencies (Jost et al., 2012; Naz et al., 2014). The problems of scale arise from the different resolutions required by glacial, nivological and hydrological processes. Physically based models that consider all glacier processes (mass balance, sub-glacial drainage and ice flow dynamics) are often too computationally expensive to be used in a combined glacio-hydrological model that considers the entire catchment. In addition, they are characterized by a complexity higher than the one of many semi-distributed hydrological models. It is therefore necessary to develop glacier models with a degree of complexity similar to the one of hydrological models but that are still able to reproduce important processes (Seibert et al., 2018).

In the present work, we give our contribution proposing a local model that follows the transformation of snow into firn and glacier ice under the influence of meteorological variables (temperature, precipitation and wind speed). Existing firn densification models are, in general, forced by snow characteristics. In this sense, the presented model allows to move the boundary of the firn densification models from surface accumulation and density to hourly meteorological series. When we do not assume stationarity in the climate, in fact, this is required to properly capture the effects of climate changes.

The core of the model was derived from mass balance, momentum balance and rheological equations, governing the evolution of snowpack and firn (depth and density of snow and firn, depth of water and refrozen meltwater and rain inside the snowpack). The calculations of the terms in the resulting equations were then approached looking at methods already used in the literature; for example, snow melt mass flux was computed with a temperature-index approach and the run-off from the snowpack with a flow matrix approach. We present two versions of the model: (1) a version (multi-layer) that considers separately each firn layer, and (2) a version (single-layer) that models firn and underlying glacier ice as a single layer. The latter consists of only six equations and it is therefore more suitable for a possible application in a hydrological model. The former consists of four equations for the snowpack plus two equations for each firn layer. Providing a profile of density with depth, it

captures better the influence of meteorological variables on snow and firn characteristics. Besides, it allows a better validation of the snow-firn model. The equations that describe the snowpack are derived from the work of De Michele et al. (2013) and later Avanzi et al. (2015), modified in order to take into account the contribution of wind erosion and the transformation of snow into firn. To model the firn component, both the densification model of Arnaud et al. (2000) and the one of Herron and
65 Langway (1980) were implemented. In order to test the model, a high altitude site, Colle Gnifetti, belonging to the Monte Rosa massif, was chosen.

The manuscript is organized as follows: we present the model in Sec. 2; illustrate the case study in Sec. 3.2; give the results in Sec. 4 and discuss them in Sec. 5. The conclusions are given in Sec. 6.

2 Methodology

70 In this section, firstly the snowpack model, proposed by De Michele et al. (2013) and later modified by Avanzi et al. (2015), with the addition of the contribution of wind to snow transport, is illustrated and secondly the model with the integration of snow and firn processes is presented.

2.1 Snow model

The snowpack is modelled, according to De Michele et al. (2013) and Avanzi et al. (2015), as a mixture of dry and wet
75 constituents. The solid deformable skeleton, that consists of both snow grains and pores, has a total volume V_S , unit area, height h_S , mass M_S and density ρ_S . The liquid water inside the pores has a volume V_W , unit area, height h_W , mass M_W and constant density $\rho_W = 1000 \text{ kg m}^{-3}$. The refrozen meltwater and rain inside the pores has a volume V_{MF} with unit area, height h_{MF} , mass M_{MF} and constant density $\rho_i = 917 \text{ kg m}^{-3}$. It is also possible to define the bulk snow density (ρ), snow water equivalent (SWE) and volumetric liquid water content (θ_W) as $\rho = (\rho_S h_S + \rho_W h_W + \rho_i h_{MF})/h$, $SWE = (\rho h)/\rho_W$
80 and $\theta_W = h_W/h$ where h is the height of the snowpack equal to $h = h_S + \langle h_{MF} + h_W - \phi h_S \rangle$ (Avanzi et al., 2015) in which ϕ is the porosity and $\langle \rangle$ are the Macaulay brackets that provide zero when the argument is negative and its value when it is positive. The height h and h_S always coincide except at the end of the snowpack existence when the liquid part and the solid part due to refreezing become predominant (i.e. $h_{MF} + h_W > \phi h_S$). In this case, $h > h_S$ because a layer of water and/or ice forms on top of the deformable skeleton.

85 The model solves the mass balance for the dry and liquid mass of the snowpack and the momentum balance and rheological equation for the solid deformable skeleton, resulting in four Ordinary Differential Equations (ODEs) in the variables h_S , h_W , h_{MF} and ρ_S . The mass fluxes considered are (1) solid precipitation events, snow melt and wind erosion for the dry snow mass, (2) rain events, snow melt, melt-freeze inside the snowpack and run-off for the liquid mass and (3) melt-freeze for the mass of ice. The dry snow density is obtained considering (1) the compaction of snow due to compaction not driven by wind (2)
90 the increase in densification rate due to drifting snow settlement and (3) a densification due to the addition of new mass. The following system is thus obtained (see Appendixes A1–A2 for the derivation of the system and the detailed description of the

terms in the equations):

$$\frac{dh_S}{dt} = -\frac{h_S}{\rho_S} \frac{d\rho_S}{dt} + \frac{\rho_{NS}}{\rho_S} s - (I \cdot a)(T_A - T_\tau) - \frac{Q}{\rho_S} \quad (1a)$$

$$\frac{dh_W}{dt} = r + \frac{\rho_S}{\rho_W} (I \cdot a)(T_A - T_\tau) + (I^* \cdot e \cdot a)(T_A - T_\tau) - \alpha \cdot K_W \quad (1b)$$

$$95 \quad \frac{dh_{MF}}{dt} = -\frac{\rho_W}{\rho_i} (I^* \cdot e \cdot a)(T_A - T_\tau) \quad (1c)$$

$$\frac{d\rho_S}{dt} = (c \cdot A_1 \cdot U) \rho_S \exp(-B \cdot (T_\tau - T_S) - A_2 \cdot \rho_S) + \frac{\rho_{NS} - \rho_S}{h_S} s \quad (1d)$$

In Eq. (1a), ρ_{NS} is the density of fresh snow (kg m^{-3}), s is the solid precipitation rate (m h^{-1}), a is a calibration parameter ($\text{m h}^{-1} \text{ } ^\circ\text{C}^{-1}$), T_A and T_τ are the air temperature and the threshold temperature for melting ($^\circ\text{C}$), I is equal to $\frac{h_S}{h_S+k}$ with $k = 0.01 \text{ m}$ if $T_A \geq T_\tau$ and zero otherwise (Avanzi et al., 2015) and Q is the mass of snow eroded by wind ($\text{kg m}^{-2} \text{ h}^{-1}$). In
 100 Eq. (1b), r is the liquid precipitation rate (m h^{-1}), e is a calibration parameter, I^* is equal to $\frac{h_W}{h_W+k}$ if $T_A < T_\tau$ and to $\frac{h_{MF}}{h_{MF}+k}$ if $T_A > T_\tau$ (Avanzi et al., 2015), $\alpha = 1.9692 \cdot 10^9 \text{ m}^{-1} \text{ h}^{-1}$ (DeWalle and Rango, 2008) and K_W is the intrinsic permeability of water in snow (m^2). In Eq. (1d), $c = 0.10 \cdot 3600 \text{ s h}^{-1}$, $A_1 = 0.0013 \text{ m}^{-1}$, $A_2 = 0.021 \text{ m}^3 \text{ kg}^{-1}$, $B = 0.08 \text{ K}^{-1}$ (Liston et al., 2007), U is the wind speed contribution (m s^{-1}) and T_S is the average snow temperature ($^\circ\text{C}$) obtained assuming thermal
 105 equilibrium between the constituents and a bilinear profile of temperature through depth (see De Michele et al. (2013) for further details).

With respect to the model by De Michele et al. (2013) and Avanzi et al. (2015), the version presented in this work includes the contribution of wind erosion to mass balance and effect of wind on densification. This is important when the model is applied to high altitude sites: Haeberli and Alean (1985), in fact, suggested that a major part of the decrease of accumulation with altitude in the Alps, that occurs above about 3500 m a.s.l., may be due to wind effects.

110 In analogy with solid transport, snow is mobilized only when wind velocity at the surface exceeds a given threshold that depends on physical properties of the surface snowpack (Li and Pomeroy, 1997). Once transport begins, snow can travel in two main modes: saltation and suspension (Déry and Taylor, 1996; Pomeroy et al., 1997). The total snow transport Q is computed by the model with the following assumptions: (1) only snow erosion occurs and no deposition of snow eroded in other positions is present; (2) measured wind speed is always referred to 10 m height, i.e. the height of the snow on the ground is neglected;
 115 (3) wind cannot erode snow that experienced a temperature greater than $0 \text{ } ^\circ\text{C}$ for the presence of ice crusts or wet layers, following Vionnet et al. (2018). These last two assumptions allow to compute the series of total snow transport Q decoupled from the snow model since knowledge of snow height is not required. In order to implement the routine we followed, with some modifications, Lehning et al. (2000), where a model of snowdrift was added to the one-dimensional snow model SNOWPACK (further details about the implementation of the routine are reported in Appendix A1).

120 2.2 Model of snow-firn dynamics

We propose here two versions of the snow-firn model. The first version (single-layer) models firn and underlying glacier ice as a single layer (Fig. 1, left panel). The resulting output is an average density and the total column height. The second version

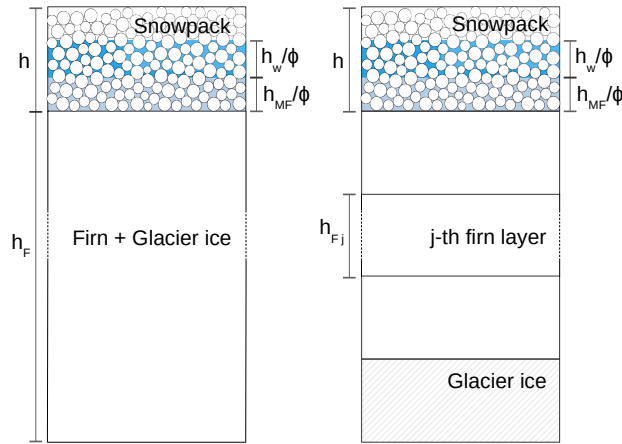


Figure 1. A column of snow, firn and ice as modelled by the single-layer (left panel) and multi-layer (right panel) version of the snow-firn model.

(multi-layer) considers separately each firn layer (Fig. 1, right panel) and it allows to distinguish between layers of firn and glacier ice. The discretized profile of density with depth can be obtained from this second implementation. The snow layer is, instead, treated as a single layer in both the two versions.

In the model we neglected the amount of water percolation inside firn. The presence of water inside firn varies greatly depending on the type of glacier. At high altitudes, where maximum temperatures are rarely positive, the effects of percolation due to melting are limited (Smiraglia et al., 2000); at the cold site of Colle Gnifetti, where the model was applied, percolation occurs only in the few centimetres below the surface and it does not involve previous year layers (Alean et al., 1983). If needed, the structure of the model allows to easily implement additional processes.

In order to separate snow from firn, we refer to its original definition according to which firn is snow that has survived one melt season (Cuffey and Paterson, 2010).

2.2.1 One-layer modelling of firn

The model is composed of two layers: the snowpack (see Sec. 2.1) and the column of firn below it. The firn is modelled as a single impermeable layer of volume V_F , unit area, height h_F , mass M_F and density ρ_F (Fig. 1, left panel).

The model consists of six ODEs: the four equations of the snow model with in addition the mass balance and momentum balance of firn. The mass variation of firn is obtained considering firn melt, the effects of precipitation on firn and the transformation of snow in firn at the end of each hydrological year. The firn densification rate is obtained considering a densification due to overburden stress and a densification due to addition of new mass. The resulting system is thus as follows (see Appendix

140 A for the derivation of the system and the detailed description of the terms in the equations):

$$\frac{dh_S}{dt} = -\frac{h_S}{\rho_S} \frac{d\rho_S}{dt} + \frac{\rho_{NS}}{\rho_S} s - (I \cdot a)(T_A - T_\tau) - \frac{Q}{\rho_S} - \sum_i h_S \delta(t - t_i) \quad (2a)$$

$$\frac{dh_W}{dt} = r + \frac{\rho_S}{\rho_W} (I \cdot a)(T_A - T_\tau) + (I^* \cdot e \cdot a)(T_A - T_\tau) - \alpha \cdot K_W - \sum_i h_W \delta(t - t_i) \quad (2b)$$

$$\frac{dh_{MF}}{dt} = -\frac{\rho_W}{\rho_i} (I^* \cdot e \cdot a)(T_A - T_\tau) - \sum_i h_{MF} \delta(t - t_i) \quad (2c)$$

$$\frac{dh_F}{dt} = -\frac{h_F}{\rho_F} \frac{d\rho_F}{dt} - (I_F \cdot a)(T_A - T_\tau) \delta(h_S) + \frac{\rho_W}{\rho_F} r \delta(h_S) \langle T_\tau - T_A \rangle + \sum_i \frac{\rho}{\rho_F} h \delta(t - t_i) \quad (2d)$$

$$145 \frac{d\rho_S}{dt} = (c \cdot A_1 \cdot U) \rho_S \exp(-B \cdot (T_\tau - T_S) - A_2 \cdot \rho_S) + \frac{\rho_{NS} - \rho_S}{h_S} s \quad (2e)$$

$$\frac{d\rho_F}{dt} = \left. \frac{d\rho_F}{dt} \right|_{comp} + \sum_i \frac{\rho - \rho_F}{h_F} h \delta(t - t_i) \quad (2f)$$

The last terms in Eqs. (2a–2c) move, at the end of each melt season, the remaining snowpack (if present) in the firn layer; t_i is the time instant at the end of hydrological year i and $\delta(\cdot)$ is the Dirac delta function. In Eq. (2d), I_F is equal to $\frac{h_F}{h_F + k}$, with k specified above, if $T_A \geq T_\tau$ and zero otherwise. In Eq. (2f), $\left. \frac{d\rho_F}{dt} \right|_{comp}$ is the densification of firn due to compaction (see Sec.

150 2.4). Equations (2a–2f) are impulsive differential equations (see e.g., Bainov and Simeonov (1993), for math details). This type of differential equations involving impulse effect are used to describe the evolution of many physical phenomena that have a sudden change in their states such as mechanical systems with impact, biological systems such as heart beats, blood flows, and population dynamics.

2.3 Multi-layer modelling of firn

155 Firn is modelled as a multi-layer column where each layer j has volume V_{Fj} , unit area, height h_{Fj} , mass M_{Fj} and density ρ_{Fj} .

The equations of the model change as follows:

$$\frac{dh_S}{dt} = -\frac{h_S}{\rho_S} \frac{d\rho_S}{dt} + \frac{\rho_{NS}}{\rho_S} s - (I \cdot a)(T_A - T_\tau) - \frac{Q}{\rho_S} - \sum_i h_S \delta(t - t_i) \quad (3a)$$

$$\frac{dh_W}{dt} = r + \frac{\rho_S}{\rho_W} (I \cdot a)(T_A - T_\tau) + (I^* \cdot e \cdot a)(T_A - T_\tau) - \alpha \cdot K_W - \sum_i h_W \delta(t - t_i) \quad (3b)$$

$$160 \quad \frac{dh_{MF}}{dt} = -\frac{\rho_W}{\rho_i} (I^* \cdot e \cdot a)(T_A - T_\tau) - \sum_i h_{MF} \delta(t - t_i) \quad (3c)$$

$$\frac{dh_{F1}}{dt} = -\frac{h_{F1}}{\rho_{F1}} \frac{d\rho_{F1}}{dt} - (I_F \cdot a)(T_A - T_\tau) \delta(h_S) + \frac{\rho_W}{\rho_{F1}} r \delta(h_S) (T_\tau - T_A) + \sum_i \frac{\rho}{\rho_{F1}} h \delta(t - t_i) - \sum_i h_{F1} \delta(t - t_i) \quad (3d)$$

$$\frac{dh_{Fj}}{dt} = -\frac{h_{Fj}}{\rho_{Fj}} \frac{d\rho_{Fj}}{dt} + \sum_i h_{F_{j-1}} \delta(t - t_i) - \sum_i h_{Fj} \delta(t - t_i) \quad (3e)$$

$$\frac{d\rho_S}{dt} = (c \cdot A_1 \cdot U) \rho_S \exp(-B \cdot (T_\tau - T_S) - A_2 \cdot \rho_S) + \frac{\rho_{NS} - \rho_S}{h_S} s \quad (3f)$$

$$\frac{d\rho_{F1}}{dt} = \left. \frac{d\rho_{F1}}{dt} \right|_{comp} + \sum_i \frac{\rho - \rho_{F1}}{h_{F1}} h \delta(t - t_i) \quad (3g)$$

$$165 \quad \frac{d\rho_{Fj}}{dt} = \left. \frac{d\rho_{Fj}}{dt} \right|_{comp} \quad (3h)$$

where j goes from two to the total number of firm layers. Firm layers that reach the ice density or whose height goes to zero are removed from the model.

2.4 Firm densification

The densification of firm due to compaction is usually subdivided into three stages: (1) a first stage dominated by the settling
170 of grains that allows to reach densities up to about 550 kg m^{-3} ; (2) a second stage dominated by sintering that extends up to
the close off density (i.e. the density at which pores become isolated) of about 830 kg m^{-3} ; (3) a last stage that ends when ice
density is reached in which further densification is driven by the compression of the bubbles of air (Cuffey and Paterson, 2010).
This last stage is in turn subdivided into two phases, depending if the pores are cylindrical or spherical. Different models of
firm densification are available in literature (see Lundin et al. (2017) for a review). Here we implemented the model of Arnaud
175 et al. (2000) with some of the modifications proposed by Bréant et al. (2017) (we will refer to it with the acronym AR) and
the model of Herron and Langway (1980) (we will refer to it with the acronym HL). Other models could also be implemented.
Both HL and AR were developed for polar sites. HL model was derived using ice cores with a mean annual firm temperature
between $-57 \text{ }^\circ\text{C}$ and $-15 \text{ }^\circ\text{C}$ and a mean annual accumulation between $0.022 \cdot 10^3 \text{ kg m}^{-2} \text{ y}^{-1}$ and $0.5 \cdot 10^3 \text{ kg m}^{-2} \text{ y}^{-1}$ while
AR model was derived from cores with a mean annual firm temperature between $-57 \text{ }^\circ\text{C}$ and $-19 \text{ }^\circ\text{C}$ and a mean annual
180 accumulation between $0.022 \cdot 10^3 \text{ kg m}^{-2} \text{ y}^{-1}$ and $1.1 \cdot 10^3 \text{ kg m}^{-2} \text{ y}^{-1}$. In the model of AR, densification equations are based
on grain sliding and creep deformations, even though maintaining empirical parameters. The model of HL consists of empirical
equations tuned with ice cores, based on the assumption that a proportionality is present between the variation in density and
the variation in stress due to new accumulation. Besides, the model of AR represents explicitly stresses while in HL the load is
parametrized through annual surface accumulation.

185 The model of HL was already applied for non polar ice cores by Huss (2013), where the model was recalibrated in order to match depth-density profiles of temperate/polythermal firn. In the presented application, the parameters were not recalibrated, despite the fact that the study site is an alpine site. This was motivated by the low mean annual firn temperature (MAFT) and low surface accumulation observed at Colle Gnifetti that resemble conditions of some polar sites.

In AR all three stages of firn densification are modelled. Equations are as follows:

$$190 \quad \left. \frac{d\rho_F}{dt} \right|_{comp} = \begin{cases} \gamma \frac{\max(P, 10^4)}{(\rho_F/\rho_i)^2} \left(1 + \frac{0.5}{6} - \frac{5}{3} \frac{\rho_F}{\rho_i}\right) \rho_i & D_D \leq \rho_F/\rho_i \leq D_0 \\ 5.3A \cdot ((\rho_F/\rho_i)^2 D_0)^{1/3} \left(\frac{a_c}{\pi}\right)^{1/2} \left(\frac{4\pi \cdot P \cdot \rho_i}{3a_c \cdot Z \cdot \rho_F}\right)^3 \rho_i & D_0 < \rho_F/\rho_i \leq D_c \\ 2A \cdot \frac{\rho_F(1-\rho_F/\rho_i)}{\rho_i(1-(1-\rho_F/\rho_i)^{1/3})^3} \left(\frac{2(P-P_b)}{3}\right)^3 \rho_i & D_c < \rho_F/\rho_i \leq 0.95 \\ \frac{9}{4}A \cdot (1-\rho_F/\rho_i)(P-P_b)\rho_i & \rho_F/\rho_i > 0.95 \end{cases} \quad (4)$$

In the first stage ($D_D \leq \rho_F/\rho_i \leq D_0$), P is the overburden pressure (Pa) and $\gamma = \gamma' \exp\left(-\frac{Q_1}{R_G(T_F+273.15)}\right)$ in which R_G is the gas constant, Q_1 an activation energy equal to $48 \cdot 10^3$ J mol⁻¹, T_F is the average temperature of firn (°C) and γ' a parameter whose value is set in order to have a continuous densification rate between the first and second stage (estimated in Sec. 4.2). D_D is the relative surface density and D_0 is the relative density at the transition between the first stage and the second stage. In the second stage ($D_0 < \rho_F/\rho_i \leq D_c$), $A = A_0 \exp\left(-\frac{Q_2}{R_G(T_F+273.15)}\right)$ with $A_0 = 2.84 \cdot 10^{-11}$ Pa⁻³ h⁻¹, a_c is the average contact area, Z is the number of particle contacts (see Appendix A3 for the expression of a_c and Z) and Q_2 is an activation energy. The value of Q_2 was set to $60 \cdot 10^3$ J mol⁻¹, as in the model of Arnaud et al. (2000), since it is the typical activation energy associated with self-diffusion of ice. However, at higher temperature (i.e. higher than -10 °C) a higher activation energy may be required to best fit density profiles with firn densification models (Cuffey and Paterson, 2010; Arthern et al., 2010; Jacka and Jun, 1994). A discussion of the thermal variation of the creep parameter and the impact of the different sintering mechanisms on it can be found in Bréant et al. (2017). Lastly, in the third stage ($\rho_F/\rho_i > D_c$), P_b is the pressure inside the bubbles equal to $P_b = P_c \frac{(\rho_F/\rho_i)(1-D_c)}{D_c \cdot (1-\rho_F/\rho_i)}$ with D_c and P_c the relative density and pressure at the transition between second and third stage. In the single-layer version, the overburden pressure P was computed as the overburden of the snowpack layer plus half of the firn layer. In the multi-layer version, we computed the overburden for each layer of firn as the overburden of the snowpack plus the overburden of all the firn layers above plus the overburden of half the firn layer considered.

In HL only the first and second densification stages are modelled. The equations are as follows:

$$\left. \frac{d\rho_F}{dt} \right|_{comp} = \begin{cases} k_0 \cdot (\omega \cdot 10^3) \cdot (\rho_i - \rho_F) & \rho_D \leq \rho_F \leq 550 \text{ kg m}^{-3} \\ k_1 \cdot (\omega \cdot 10^3)^{0.5} \cdot (\rho_i - \rho_F) & 550 < \rho_F < 800 \text{ kg m}^{-3} \end{cases} \quad (5)$$

where $k_0 = 11 \exp\left(-\frac{10160}{R_G(T_F+273.15)}\right)$, $k_1 = 575 \exp\left(-\frac{21400}{R_G(T_F+273.15)}\right)$ and ω is the annual snow accumulation (kg m⁻² y⁻¹). In HL the transition density between first and second stage is fixed and equal to 550 kg m⁻³. In order to run the model of HL in a dynamic way, for each year we computed the annual accumulation averaging the ones modelled between the year of deposition of the firn layer and the year before the one considered, following Stevens et al. (2020).

Steady-state firn densification models are not applied to the superficial snow where the metamorphism is more complex and significantly influenced by air temperature. The original model of Arnaud et al. (2000), for example, was used only for depths higher than 2 m. In this case, we applied them only for densities higher than a density ρ_D , that represents the average snow density. For firn densities lower than ρ_D , the densification equation of snow was adopted but neglecting wind contribution. In this way, the transition between the two equations is driven by density rather than being associated with the end of a water year. This is important, for example, when consistent fresh snow falls over the snowpack at the end of the hydrological year.

2.4.1 Temperature profile

The energetic description of the volume was simplified assuming the constituents in thermal equilibrium and assuming a bilinear profile of temperature through depth. Temperature was assumed to vary linearly from the surface temperature T_0 to the MAFT at the depth z_M at which seasonal variation of temperature is negligible. Below z_M , temperature was kept constant and equal to MAFT. In cold glaciers the value of MAFT is close to the mean annual air temperature (MAAT) when melt water percolation is limited (Suter et al., 2001) while in temperate glaciers it is equal to the melting temperature (Cuffey and Paterson, 2010). Surface temperature was fixed equal to T_A if $T_A < 0^\circ\text{C}$ and zero elsewhere. Already Huss (2013) assumed a bilinear profile of temperature in order to study temperate firn densification, fixing z_M to 5 m since it is the typical penetration of winter air temperature. The temperature profile was then used to compute the average snow and firn temperatures that influence snow and firn densification.

2.5 Numerical model

The model was solved using the forward Euler method with a constant step size, Δt , of one hour. To compute the last terms in Eqs. (1d), (2f) and (3g) also when h_S , h_F and h_{F_1} are zero, these terms were calculated, following De Michele et al. (2013), as $\frac{\rho_{NS}(t)-\rho_S}{h_S(t)+s(t)\Delta t} s(t)$, $\frac{\rho(t)-\rho_F}{h_F(t)+h(t)} \frac{h(t)}{\Delta t}$ and $\frac{\rho(t)-\rho_{F_1}}{h_{F_1}(t)+h(t)} \frac{h(t)}{\Delta t}$. Regarding the vertical discretization, the firn component of the multi-layer version of the model was discretized modelling one layer for each hydrological year.

3 Study area and data

In the following section we will present the study area (Sec. 3.1), the data collection and handling (Sec.s 3.2–3.3) and eventually the calibration and site specific parameters (Sec.s 3.4–3.5).

3.1 Study area

The site of Colle Gnifetti (CG) is part of the summit ranges of the Monte Rosa massif, Swiss/Italian Alps. It is the uppermost part of the accumulation area of Grenzgletscher and it forms a saddle that lies between Signalkuppe (4554 m a.s.l.) and Zumsteinspitze (4563 m a.s.l.) at an altitude of 4400–4550 m a.s.l. (Lüthi and Funk, 2000) (Fig. 2). The glacier at Colle Gnifetti has a thickness between 60 and 120 m and a MAFT of -14°C (Wagenbach et al., 2012). The regime is that of a high altitude site, i.e. nearly persistent sub-zero air temperature, a high precipitation total and high wind speed (Suter et al., 2001).

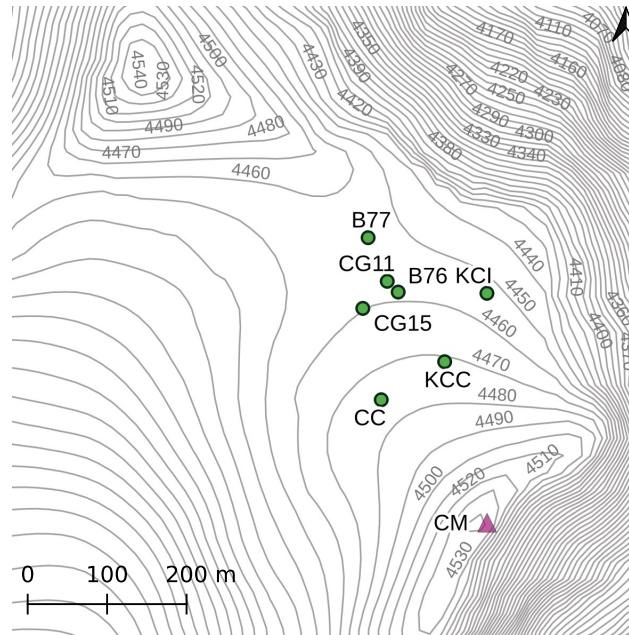


Figure 2. The site of Colle Gnifetti and the location of the ice cores considered in the present work. CG03 and CG15 ice core share the same location therefore CG03 is not shown. The position of Capanna Regina Margherita (CM) is also shown.

A mean annual precipitation of $2.7 \cdot 10^3 \text{ kg m}^{-2} \text{ y}^{-1}$ with an interannual variability of $0.8 \cdot 10^3 \text{ kg m}^{-2} \text{ y}^{-1}$ (Mariani et al., 2014) was estimated for the period 1961–1993 from a core extracted at upper Grenzgletscher (Eichler et al., 2000).

245 Even though the site is characterized by high precipitation totals, accumulation in the saddle is considerably lower and highly variable over the glacier surface due to wind erosion, with values ranging from about $0.15 \cdot 10^3 \text{ kg m}^{-2} \text{ y}^{-1}$ to $1.2 \cdot 10^3 \text{ kg m}^{-2} \text{ y}^{-1}$ depending on the wind exposure (Alean et al., 1983; Lüthi and Funk, 2000; Licciulli et al., 2020). Alean et al. (1983) measured the accumulation at CG between 17 August 1980 and 23 July 1982 with a network of 30 stakes. For the period between 14 August 1981 and 23 July 1982 the mass balance was negative in all the stakes due to wind erosion, while the net
 250 accumulation of hydrological year 1980–1981 varied between $+0.04 \cdot 10^3 \text{ kg m}^{-2} \text{ y}^{-1}$ and $+1.18 \cdot 10^3 \text{ kg m}^{-2} \text{ y}^{-1}$ with the highest values on south facing slopes. This occurs because the enhanced melting and refreezing causes the formation of wet layers and ice crusts and because higher temperatures are associated with a faster densification and both these aspects reduce the possibility of wind to erode snow. This results also in the fact that almost all the snow that survives the melt season comes from summer events (Bohleber et al., 2018; Schöner et al., 2002).

255 3.2 Data collection

The stations whose data were used in this study are presented in Fig. 3 and they are summarized in Table 1. Hourly data of air temperature and wind speed at Capanna Regina Margherita (CM) were used as input for the model, hourly data at Passo del Moro (PM) to reconstruct precipitation at CM and hourly and daily air temperature data at Macugnaga Pecetto (MP),

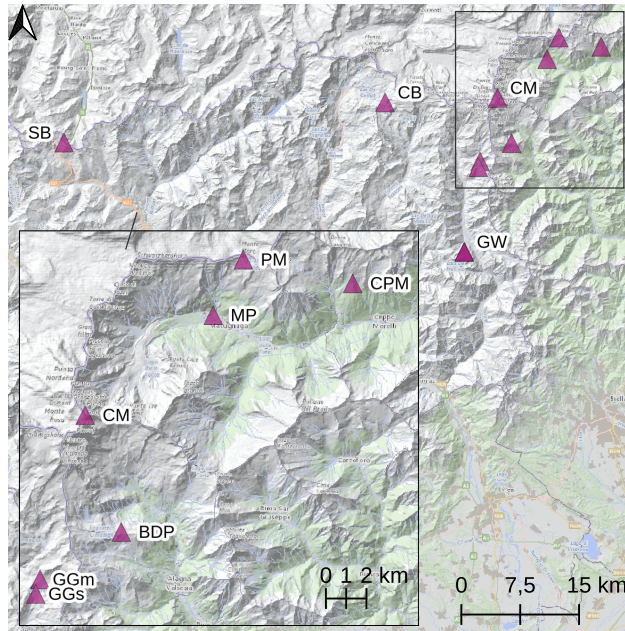


Figure 3. Location of the meteorological stations used: Capanna Regina Margherita (CM), Macugnaga Pecetto (MP), Ceppo Morelli (CPM), Passo del Moro (PM), Bocchetta delle Pisse (BDP), Col du Grand St Bernard (SB), Valtournenche-Cime Bianche (CB), Gressoney-la-Trinité - Gabiet (GGm and GGS) and Gressoney-Saint-Jean - Weissmatten (GW). The location of the meteorological station at Weissmatten and the location of snow measurements are only few meters apart so only one point is reported. In the bottom left panel a zoom over some stations is included. All stations belong to Arpa Piemonte with the exclusion of CB, GG and GW that belong to the Aosta Valley Region and SB that belongs to the National Oceanic and Atmospheric Administration (NOAA). Source of the basemap: Arpa Piemonte Geoportale.

Passo del Moro, Bocchetta delle Pisse (BDP) and Ceppo Morelli (CPM) to infill missing temperature data at Capanna Regina Margherita. Hourly wind speed data at Valtournenche-Cime Bianche (CB) and Col du Grand St Bernard (SB) were used to infill missing wind speed data at CM. Hourly data at the meteorological stations of Gressoney-Saint-Jean - Weissmatten (GWm) and Gressoney-la-Trinité - Gabiet (GGm) and snow water equivalent data (GWs and GGS) were used to calibrate and validate the parameter a and e of the snow model. Snow water equivalent is measured by the Aosta Region during winter both at fixed locations and at itinerant sites. For GGs, four years of measurements were available with in average 24 data for each winter. For GWs, five years were available with in average eight data for each winter.

The station of Capanna Regina Margherita, whose data were used to run the snow-firn model, was installed in 2002 by the Piedmont Region at the Regina Margherita Hut as part of a project that aimed to study the interaction between synoptic flow and orography. With its 4560 m of altitude, it can be considered the highest meteorological station in Europe and its wind speed series can be considered representative of the synoptic conditions (Martorina et al., 2003). Due to its recent installation, the use of these data limits the length of the simulation and the number of cores with which our results can be compared. Nevertheless, we believe that, given the peculiar characteristics of the station, the use of these data may give added value to this study.

Table 1. Meteorological data employed in the case study (p stands for precipitation, SD for snow depth, T_A air temperature, u average wind speed and s fresh snow). Hydrological years are identified by the last year, e.g. 2009 is hydrological year 2008–2009. With hydrological year we refer to the period from 1 October to 30 September of the next year.

Station name	Altitude (m a.s.l.)	UTM X WGS84 (m)	UTM Y WGS84 (m)	Variable	Aggregation	Period used	Source
Capanna Regina Margherita (CM)	4560	412930	5086564	T_A, u	Hourly	1 October 2002– 13 August 2013	Arpa Piemonte
Passo del Moro (PM)	2820	420739	5094227	T_A	Daily	1 October 2002– 30 September 2007	Arpa Piemonte
Passo del Moro (PM)	2820	420739	5094227	$p, SD, T_A, u,$	Hourly	1 October 2002, 30 September 2019	Arpa Piemonte
Bocchetta delle Pisse (BDP)	2410	414709	5080807	T_A	Daily	1 October 2002– 30 September 2007	Arpa Piemonte
Bocchetta delle Pisse (BDP)	2410	414709	5080807	T_A	Hourly	November 2002, September 2007	Arpa Piemonte
Ceppo Morelli (CPM)	1995	426141	5093057	T_A	Daily	1 October 2002– 30 September 2007	Arpa Piemonte
Ceppo Morelli (CPM)	1995	426141	5093057	T_A	Hourly	November 2002, September 2007	Arpa Piemonte
Gressoney-la-Trinité Gabiet (GGm)	2379	410705	5078465	p, SD, T_A, u	Hourly	1 October 2017 30 September 2021	Aosta Valley Region
Gressoney-la-Trinité Gabiet (GGs)	2340	410490	5077754	SWE	Not fixed	Water years: 2018, 2019 2020, 2021	Aosta Valley Region
Gressoney-Saint-Jean Weissmatten (GWm)	2038	408692	5066969	p, SD, T_A, u	Hourly	1 October 2015 30 September 2020	Aosta Valley Region
Gressoney-Saint-Jean Weissmatten (GWs)	2035	408686	5066982	SWE	Not fixed	Water years: 2016, 2017 2018, 2019, 2020	Aosta Valley Region
Valtournenche Cime Bianche (CB)	3100	398610	5085987	u	Hourly	1 October 2003, 30 September 2019	Aosta Valley Region
Col du Grand St Bernard (SB)	2479	357703	5080871	u	Hourly	1 October 2002, 30 September 2019	NOAA

In Table 2 ice core data are reported (Fig. 2). Available data consist of some or all of the following information: depth in meters, depth in meters of water equivalent, density and dating. We recall that the first three variables are related, so that one of them can be computed given the other two.

Table 2. Ice core data employed in the case study.

Name	Drilling date	Mean annual accumulation ($10^3 \text{ kg m}^{-2} \text{ y}^{-1}$)	Data source
B76	1976	0.37	Gäggeler et al. (1983)
B77	1977	0.32	Gäggeler et al. (1983)
CG03	2003	0.45	Sigl et al. (2018)
CG15	2015	0.45	Sigl et al. (2018)
CG11	2011	0.41	Ardenghi (2012)
CC	1982	0.22	Licciulli et al. (2020)
KCI	2005	0.14	Licciulli et al. (2020)
KCC	2013	0.22	Licciulli et al. (2020)

275 3.3 Data handling

The model requires as input a continuous series of air temperature, precipitation and wind speed.

Following the comparison presented by Henn et al. (2013), to fill missing hourly temperature data at Capanna Margherita, the MicroMet preprocessor (Liston and Elder, 2006) was adopted for gap smaller than 24 hours and a long-term lapse rate approach with five stations (CM, MP, CPM, PM, BDP) was adopted for longer gaps. MicroMet is a meteorological model
 280 that includes a data-fill procedure here adopted. The method distinguishes between three conditions: (1) for 1 h gaps the missing information is replaced with the average of the previous and next measurement; (2) for 2–24 h gaps each missing value is replaced with the average of the values recorded the next and previous day at the same hour; (3) for longer gaps an auto regressive integrated moving average (ARIMA) model is used (Hyndman and Athanasopoulos, 2018). Here, for the third condition, the long-term lapse rate approach was used, as specified above. In the period 1 October 2002–13 August 2013,
 285 0.37 % of hourly temperature data were missing. After MicroMet procedure 0.23 % remained missing and were substituted with a long-term lapse rate approach.

Wind speed data measured at CM are characterized by repeated zero values that are not observed in near stations and that are probably due to the freezing of the anemometer. In the period 1 October 2002–13 August 2013 nearly 30 % of the wind speed data at CM were equal to zero, while 1.3 % were missing. By comparison, in the same period, there were 2 % zero
 290 values in SB series. These zero values were therefore considered missing. To fill missing wind speed data at CM, MicroMet procedure was used for gaps smaller than 24 hours. For gaps longer than 24 hours, data were replaced using measurements at CB or, if wind speed data were missing also at CB, with data measured at SB. In both series, zero wind speed values recorded for more than four consecutive hours were set missing. In order to take into account the different characteristics of the sites we first computed for each of the three stations the mean and standard deviation for each hour of the year and we removed it from
 295 the data. Missing data at CM were first replaced with the corresponding residual value measured at CB (or SB) and then the

final value was obtained using the mean and standard deviation estimated at CM. Reconstructed negative wind speed values at CM were set to zero. Missing wind speed data at CM were set to zero if they were zero at CB (or SB).

The precipitation series at CM was reconstructed using hourly data measured at PM. The station was chosen due to its vicinity to CM and its altitude of 2820 m a.s.l.. Using the formula proposed by Alpert (1986) and considering a bell shaped mountain, we estimated for the Monte Rosa massif an altitude of maximum precipitation of $z_m = 2547$ m. The altitude of maximum precipitation is away from the crest as it is typical for large mountains (Roe, 2005). We therefore expect to have similar precipitation totals at CM and PM. The precipitation series measured at PM needs to be integrated with snow depth data since the pluviometer undercatches or does not catch solid precipitation events in winter. In order to reconstruct the total precipitation series, we followed the routine presented by Avanzi et al. (2014). Solid precipitation is obtained looking at the positive variations in snow depth data, while rainfall is given by the difference, if positive, between total precipitation and solid precipitation. Positive variations of snow depth, however, may also be recorded when strong temperature variations occur, thus introducing false events. Unlike Avanzi et al. (2014), we approached this problem smoothing the snow depth series with a moving average whose window size was calibrated running the snow model at PM and looking for the best match between simulations and observations. Even though PM has an altitude higher than the estimated altitude of maximum precipitation, we obtained a mean annual precipitation of about $2 \cdot 10^3 \text{ kg m}^{-2} \text{ y}^{-1}$ for the period 2002–2019, lower than the one estimated at CG by Mariani et al. (2014). We suppose this may be due to wind erosion events; the procedure implemented by Avanzi et al. (2014), in fact, may compensate for snow depth variations due to wind erosion decreasing the estimated solid precipitation. We therefore increased the resulting hourly solid precipitation with a constant factor in order to match the observed mean annual accumulation at CG of $2.7 \cdot 10^3 \text{ kg m}^{-2} \text{ y}^{-1}$. The total precipitation series was then divided between solid and liquid precipitation using a threshold of 1°C since this is the value generally found in Europe (Jennings et al., 2018).

3.4 Calibration of model's parameters

The model requires the calibration of three parameters, namely a and e in Eq.s 1a–1c and γ' in Eq. 4.

The parameters a and e were calibrated running the snow model, with the addition of the wind module, at GW, with an hourly time step from 1 October 2015 to 30 September 2020. Input series were processed as reported for PM in Sec. 3.3. The parameter a governs the amount of snowmelt, and consequently snow height, and the relative amount of snow and ice inside the snowpack, thus influencing snow water equivalent and density. On the contrary, the parameter e influences only the relative amount of snow and ice inside the snowpack and does not contribute to snow height. The calibration problem is therefore a multi objective one, since we could optimize the error both on snow height and density or *SWE*. We decided to move from a multi objective to a single objective optimization problem, aggregating the NSE (Nash-Sutcliffe Efficiency) between observed and simulated snow depth data and the NSE between observed and simulated snow water equivalent data. We calculated the error metrics considering together all the available years but computing the measure only in the periods with snow depth higher than zero and we aggregated them giving a weight of 0.7 to the first and 0.3 to the second. In this way we took into account the higher uncertainty in *SWE* data due to the shorter sample length and the non coincidence between the location of the meteorological station and the snow measurements. The optimum parameters were then estimated for different moving

330 average windows, used to process solid precipitation input data, with the use of a population-evolution-based algorithm, namely
SCE-UA (Shuffled Complex Evolution-University of Arizona) (Duan et al., 1992, 1993). We thus obtained a pair of a and e for
each window and we selected the one maximizing the objective function. The validation was performed applying the model
with the selected set of parameters at GG for the period 1 October 2017 – 30 September 2021.

335 The parameter γ' , that governs firm densification rate in AR, was chosen in order to have a continuous densification rate
between first and second stage of densification. For each of the available ice cores, with the exception of CG11, we computed
the parameter γ' running AR in a steady-state condition (Bader, 1954) using the mean accumulation reported in Table 2. In
addition, the parameters of the firm densification model chosen may need calibration if applied to sites significantly different
from the polar ones.

3.5 Site specific parameters

340 In order to apply AR we set $D_0 = 0.56$ (Bréant et al., 2017), $P_c = 740 \cdot 10^2$ Pa (Lüthi and Funk, 2000) and $D_c = 0.9$ since the
precise value is not known at CG (Lüthi and Funk, 2000). Two different firm temperatures, $T_F = -14$ °C and $T_F = -10$ °C,
that cover the observed ice temperatures at CG (Lüthi and Funk, 2000), were tested together with different surface densities,
chosen looking at values already used in literature at CG. We selected three values: $\rho_D = 300$ kg m⁻³, $\rho_D = 360$ kg m⁻³ and
 $\rho_D = 410$ kg m⁻³, the values already assumed by Licciulli et al. (2020) and Lüthi and Funk (2000). The model of AR was run
345 with a slight modification. We used the first stage densification equation up to a relative density of 0.6, but we kept $D_0 = 0.56$ in
the second stage densification equation. The latter, in fact, cannot be applied for $D = D_0$ and it gives densification rates tending
to infinity for values tending to D_0 . The other site specific parameters of the snow-firm model that require to be specified are
 z_M , set to 5 m (Haeberli and Funk, 1991), and the grain radius R , that influences the threshold wind speed. It is defined as
 $R = 3/(\rho_i SSA)$ where SSA is the specific surface area in m² kg⁻¹. SSA was computed adopting the parametrization of
350 Domine et al. (2007) for recent snow, $SSA = -16.051 \ln(\rho_S \cdot 10^{-3}) + 7.01$.

4 Results

4.1 Parameters' estimation

We obtained a value of the parameters a and e of $2.94 \cdot 10^{-4}$ m h⁻¹ °C⁻¹ and 0.164, respectively. The combined NSE in
calibration is 0.82, with a NSE of 0.84 and 0.78 for snow depth and snow water equivalent data, respectively. In validation,
355 the combined NSE and the NSE for snow depth and snow water equivalent are respectively 0.77, 0.84 and 0.61. We also
computed the RMSE and MBE in validation, that are equal to $0.126 \cdot 10^3$ kg m⁻² y⁻¹ and $0.0116 \cdot 10^3$ kg m⁻² y⁻¹ for snow
water equivalent and 0.26 m and 0.0672 m for snow depth. Avanzi et al. (2014) estimated the parameter a for a selection of
forty sites with altitudes between 91 and 3389 m a.s.l. within the SNOTEL (Snow Telemetry) network, a network of automated
stations, located in mountain basins of western U.S., operated by the Natural Resources Conservation Service (NRCS). They

Table 3. Modelled and observed mean (μ) and standard deviation (σ) of the accumulation rate for the period 2003–2010.

	μ ($10^3 \text{ kg m}^{-2} \text{ y}^{-1}$)	σ ($10^3 \text{ kg m}^{-2} \text{ y}^{-1}$)
Model	0.49	0.15
CG11	0.41	0.09
KCC	0.31	0.09
CG15	0.38	0.16

360 obtained median values between $1 \cdot 10^{-4} \text{ m h}^{-1} \text{ }^\circ\text{C}^{-1}$ and $6 \cdot 10^{-4} \text{ m h}^{-1} \text{ }^\circ\text{C}^{-1}$. Regarding the parameter e , values of 0.2 and 0.25 were estimated by Avanzi et al. (2015) for two sites in Japan.

4.2 Steady-state firn densification

The depth density profiles obtained using the model of AR and HL in a steady-state condition are reported in Fig. 4 for a surface density $\rho_D = 360 \text{ kg m}^{-3}$. Both HL and AR have very good performances when applied to KCC ice core. The worst
365 performances occur for CG03 with an underestimation of densification rate for all depths. For the remaining ice cores the models of AR and HL have a good fit up to depths of about 20–30 m, but they underestimate densification rate below it. The profiles show in general a better performance of HL. We recall that the model of HL was derived considering also cores with MAFT and accumulation close to the ones of CG, while AR was optimized for cores with lower MAFT.

4.3 Snow accumulation

370 The annual accumulation obtained from the snow-firn model is reported in Fig. 5, along with the values retrieved from the three available ice cores, the average value of the observations and its 95% confidence interval. The RMSE between the model and the average of the observations is equal to $0.22 \cdot 10^3 \text{ kg m}^{-2} \text{ y}^{-1}$, while the modelled and observed average annual accumulation and standard deviation are reported in Table 3.

In order to better understand the characteristics of the accumulation at CG, the monthly box plot of snow transport, solid
375 precipitation, number of hours with $T_A > 0 \text{ }^\circ\text{C}$, that in the model correspond to hours with melting, and monthly contribution to annual accumulation, computed for each month as $100 \times (\text{solid precipitation} - \text{eroded snow}) / \text{solid precipitation}$, are provided in Fig. 6. Since snow is moved into firn at the end of September and wind is not allowed to erode firn, the fraction of conserved snow of September may be overestimated and the snow transport of October underestimated. We can see that annual accumulation is composed by snow deposited mainly between April and September, with June the month that in average
380 contributes the most. The months in which solid precipitation is conserved are also the months in which temperature goes above the melting point; winter snow, instead, is completely removed.

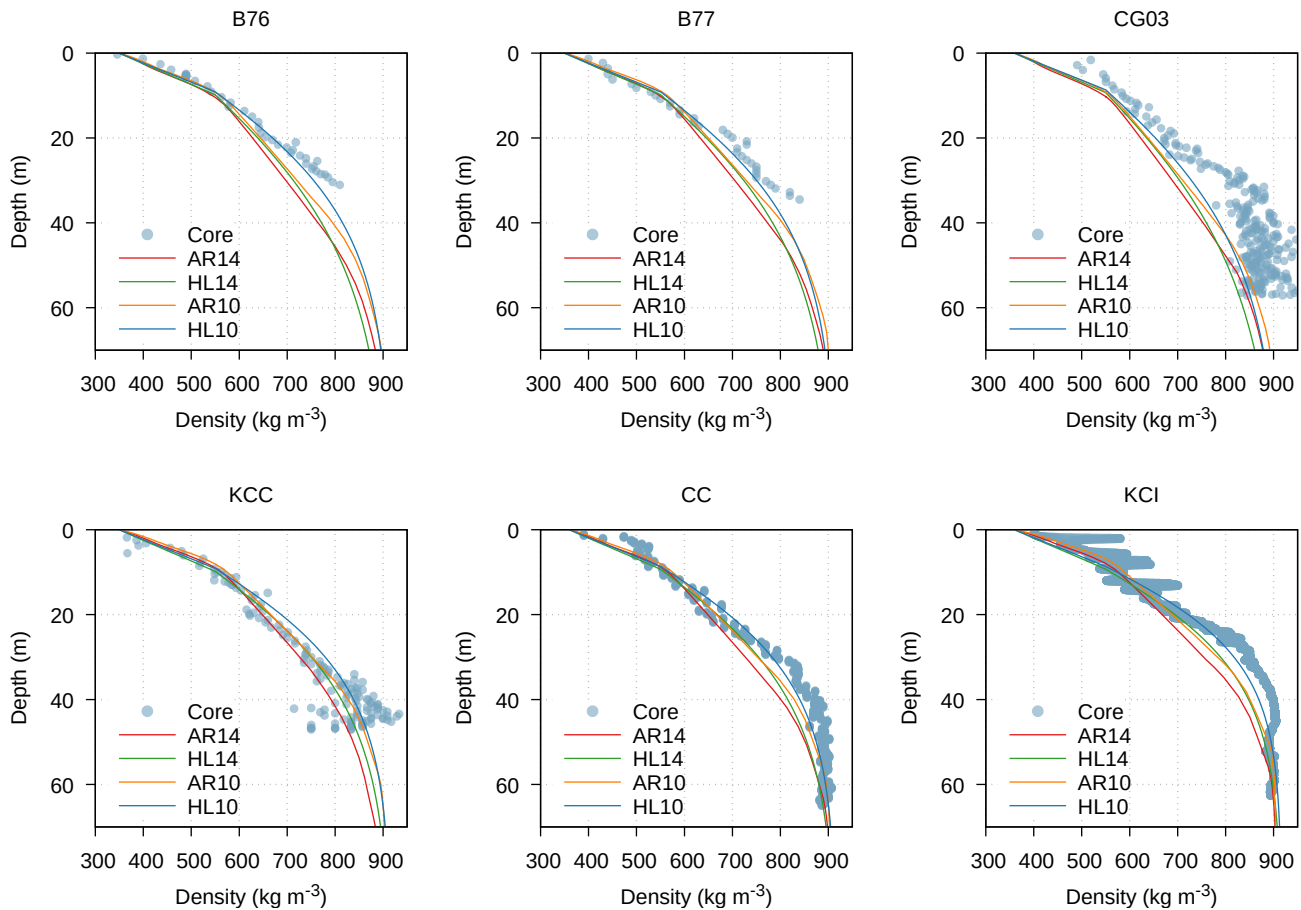


Figure 4. Observed and modelled depth density profiles. Modelled profiles are obtained running Arnaud et al. (2000) (AR) and Herron and Langway (1980) (HL) in a steady-state condition. The numbers 14 and 10 stand for a mean annual firn temperature of $-14\text{ }^{\circ}\text{C}$ and $-10\text{ }^{\circ}\text{C}$, respectively.

4.4 Firn density

4.4.1 One-layer model version

385 The modelled firn density was confronted with the density estimated from KCC and CG15 ice cores. With the one-layer version, we obtain one average value of firn density for each run of the model. We therefore run the model multiple times, fixing the end year of the simulation to the date of the core drilling and anticipating at each run the starting date of one year. For each run, the corresponding observed firn density was obtained averaging the density profile of the ice core associated to

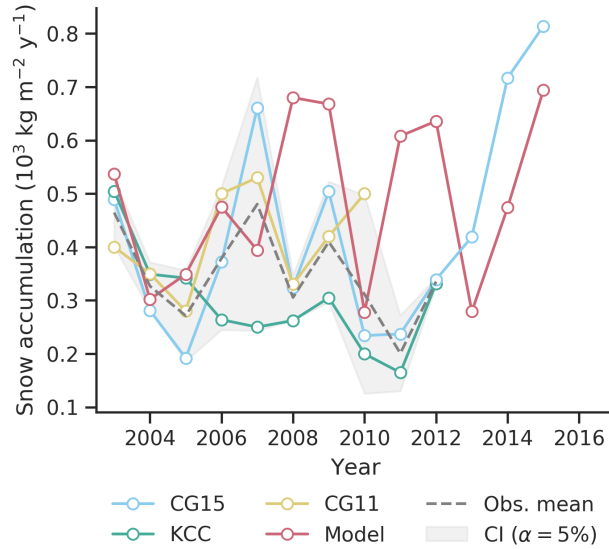


Figure 5. Annual accumulation modelled and retrieved from three ice cores. The average of the annual accumulations from ice cores and its 95% confidence interval are also reported.

the same range of years. The results obtained implementing both AR and HL are reported in Fig. 7. For KCC we fixed the MAFT to $-14\text{ }^{\circ}\text{C}$, while for CG15 to $-10\text{ }^{\circ}\text{C}$, looking for the best performance in Fig. 4.

390 Regarding firn density, we have contrasting results depending on the core and the densification model adopted. Both model versions overestimate KCC density with a better performance when AR is implemented, on the contrary we obtained an underestimation of CG15 average density, with a better performance when HL is implemented. In all the combinations, however, we observed a reduction in the error when more firn layers are averaged.

Moving to firn depth, the model nearly always predicts higher depths, with more significant differences for KCC ice core.

395 4.4.2 Multi-layer model version

The modelled density profile was compared with KCC and CG15 density data, implementing in the model both AR and HL (Fig. 8) and testing three different transition densities between snow and firn. Profiles are reported as steps, where each step corresponds to a firn layer. Focusing on CG15 ice core, we modelled, with both versions, lower densities in the first 4–5 m, with a layer with a particular low density not matched by the ice core data at around 1–2 m from the surface. This marked decrease however is reduced when a $\rho_D = 410\text{ kg m}^{-3}$ is chosen. For higher depths, the model with AR still underestimates CG15 density, while with HL a better match of the profile is observed. The best performance is obtained implementing HL and selecting $\rho_D = 410\text{ kg m}^{-3}$, with a mismatch only in the first meters.

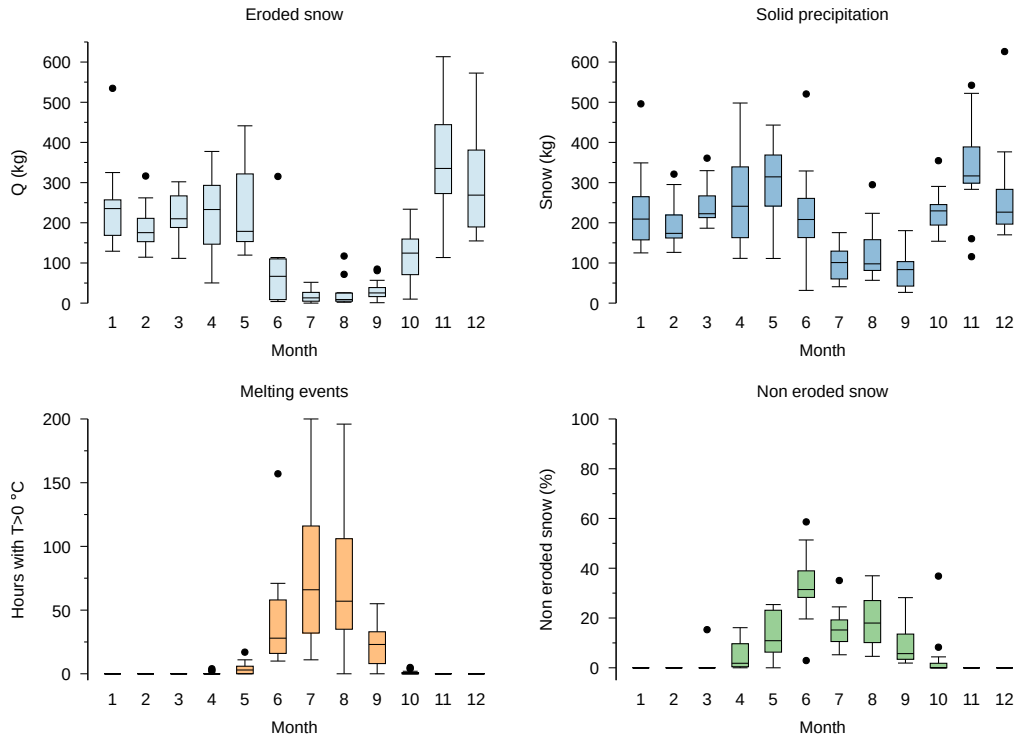


Figure 6. Box plot of monthly eroded snow (top left), monthly solid precipitation (top right), monthly number of hours with above zero temperatures (bottom left) and monthly fraction of conserved solid precipitation (bottom right), obtained for the period 1 October 2002–30 September 2015. The horizontal bar inside the box is drawn at the median while the upper and lower ends of the box are drawn at the upper and lower quartile, respectively. The vertical lines, called whiskers, extend up to the most distant point that has a value within 1.5 of the interquartile range. The points outside these limits are drawn individually with dots.

Moving to KCC ice core, the model with implemented AR results in an overestimation of density up to a depth of around 4 m and an underestimation below it. Implementing HL, the density is instead overestimated except for a layer at around 8 m of depth.

4.5 Comparison between multi- and single-layer model versions

In order to understand the approximation introduced modelling firm as a single layer instead of a multi-layer column, we compared in Figs 9–10 the average firm density obtained with the single-layer version of the model or averaging the density of each individual firm layer obtained with the multi-layer version, weighted for their height. The results for $\rho_D = 300 \text{ kg m}^{-3}$ are not reported since they were not significantly different from the one with $\rho_D = 360 \text{ kg m}^{-3}$. Setting $\rho_D = 360 \text{ kg m}^{-3}$, we have, implementing HL, a maximum difference between the two average densities of 16.7 kg m^{-3} , obtained for KCC ice core, while implementing AR of 7 kg m^{-3} for CG15 ice core. Higher differences are obtained moving to $\rho_D = 410 \text{ kg m}^{-3}$, with a

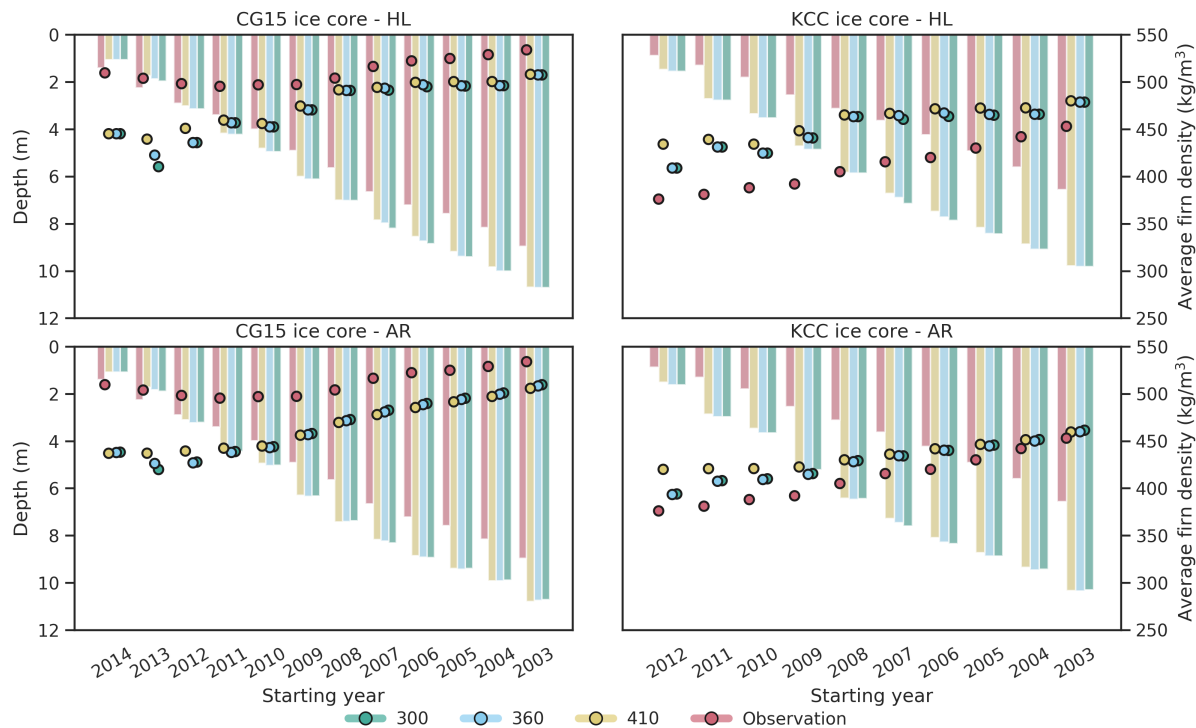


Figure 7. Observed and modelled (with one-layer version) average firn density (dots, right axis) and depth (bars, left axis) for KCC and CG15. Each cluster corresponds to a run of the model whose starting date is reported on the x-axis. Ending year for all runs is 30 August 2013 for KCC and 30 September 2015 for CG15. AR and HL stand for the model version with Arnaud et al. (2000) and Herron and Langway (1980) implemented, respectively. The values 300, 360 and 410 stand for the chosen value of ρ_D .

maximum difference of 29 kg m^{-3} and 14 kg m^{-3} implementing HL and AR, respectively, obtained for KCC ice core. In all cases the multi-layer version predict higher average densities.

415 5 Discussion

5.1 Steady-state firn densification

Figure 4 shows a variable performance of the firn densification model depending on the ice core considered; with the exception of KCC and CG15 that show respectively a very good and a very poor performance, for all the other cores we have a good fit up to a density of about $600\text{--}700 \text{ kg m}^{-3}$. Also Bréant et al. (2017), that modified the original model of AR, observed a
 420 variable agreement between data and model, also for sites with similar accumulation and temperature. They suggested that this may be due to different flow regimes of the sites, since their 1D model does not include this effect. Another consideration that emerges from Fig. 4, pointed out also by Bréant et al. (2017), is that the modelled profile results in worse performances when

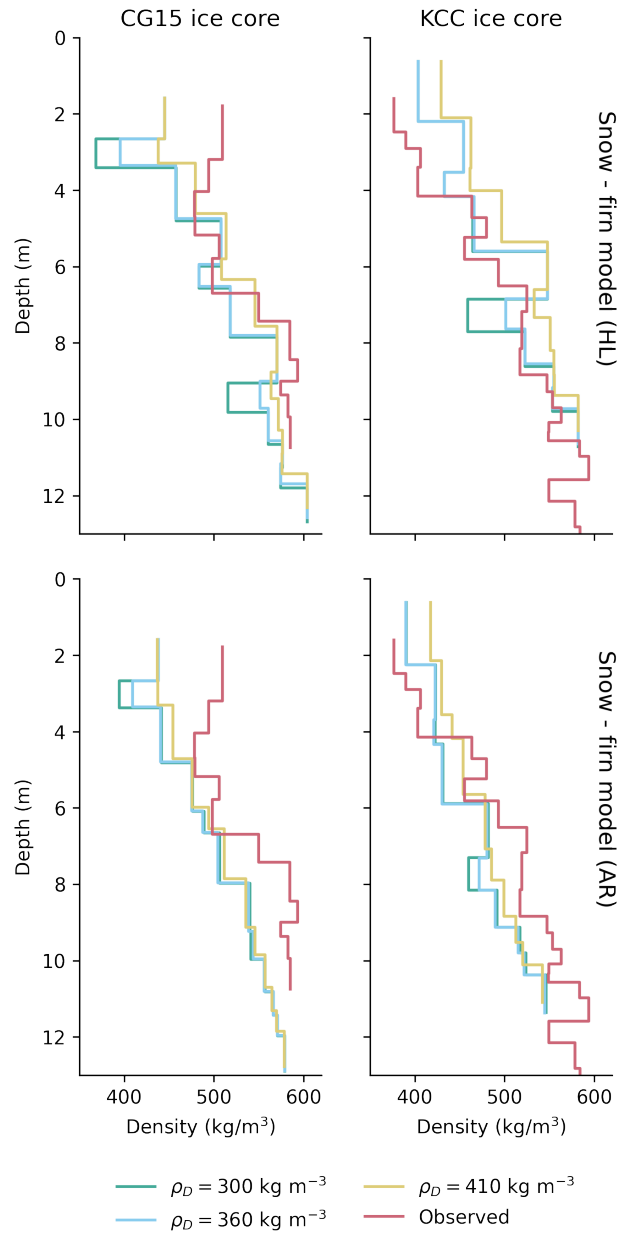


Figure 8. Observed and modelled (with multi-layer version) firn density profiles for KCC (bottom panels) and CG15 (top panels). AR and HL stand for the model version with Arnaud et al. (2000) and Herron and Langway (1980) implemented, respectively.

the observed density profile does not show a clear change in densification rate near the critical density D_0 . The transition is, in fact, more evident for KCC ice core that is associated with the best fit. Finally, Bréant et al. (2017) reported a tendency of the model to overestimate densification rate for lower densities and to underestimate it for higher densities. This is coherent with

425

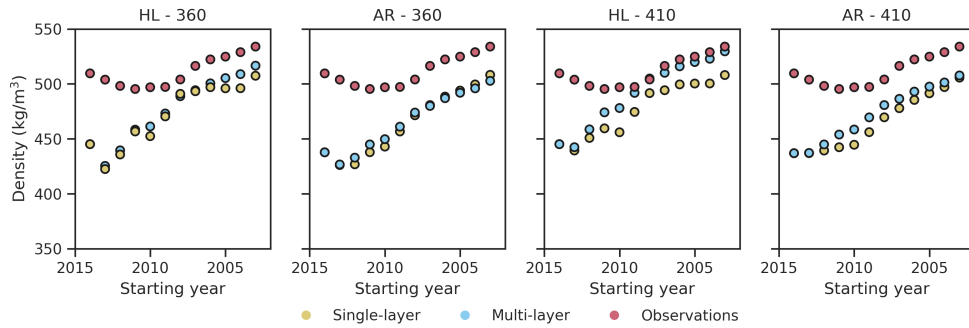


Figure 9. Average firn density of CG15 ice core observed and obtained with the single-layer version of the model or averaging the density of each individual firn layer obtained with the multi-layer version, weighted for their height. Each point corresponds to a run of the model whose starting date is reported on the x-axis. Ending year for all runs is 30 September 2015. AR and HL stand for the model version with Arnaud et al. (2000) and Herron and Langway (1980) implemented, respectively. The values 360 and 410 stand for the chosen value of ρ_D .

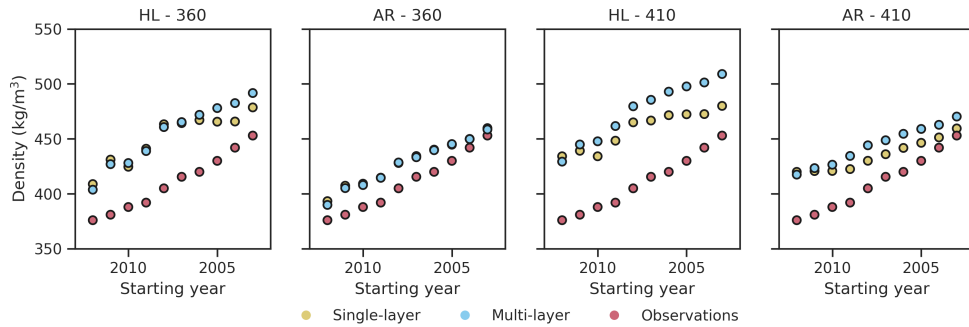


Figure 10. Average firn density of KCC ice core observed and obtained with the single-layer version of the model or averaging the density of each individual firn layer obtained with the multi-layer version, weighted for their height. Each point corresponds to a run of the model whose starting date is reported on the x-axis. Ending year for all runs is 30 August 2013. AR and HL stand for the model version with Arnaud et al. (2000) and Herron and Langway (1980) implemented, respectively. The values 360 and 410 stand for the chosen value of ρ_D .

the results obtained, for which HL predicts lower densities before D_0 and higher densities after D_0 , if compared with AR. In order to compare modelled and observed profiles in Fig. 4 it is important to point out that the two models assume stationary conditions, therefore they are not able to reproduce possible changes in the glaciological characteristics. In some of the ice cores it is possible to see a bend in the profile in correspondence of of about 20–30 m. The reason could be a combination of ice flow and the upstream-effect, i.e. changes in snow accumulation upstream, and these effects can not be reproduced by a 1D model like the ones used.

5.2 Snow accumulation

Snow accumulation at CG is characterized by a high spatial variability (Keck, 2001; Licciulli et al., 2020). The difference in net annual accumulation of CG11 and CG15, that are about 50 m apart, ranges from $+0.13 \cdot 10^3 \text{ kg m}^{-2} \text{ y}^{-1}$ to $-0.266 \cdot 10^3 \text{ kg m}^{-2} \text{ y}^{-1}$ in the period 2002–2012, while the one of CG15 and KCC, that are about 120 m apart, ranges between $+0.41 \cdot 10^3 \text{ kg m}^{-2} \text{ y}^{-1}$ and $-0.15 \cdot 10^3 \text{ kg m}^{-2} \text{ y}^{-1}$. Given the high variability in the accumulation rate, three ice cores may not be enough to fully represent the site. In addition, ice core data are biased due to the fact they are drilled preferentially in the north flank, where accumulation is lower. While the modelled average annual accumulation is in the range of the ones estimated for the north flank of CG (Licciulli et al., 2020), the model is not able to reproduce the observed spatial variability. Due to the lack of dependence on topography in the presented model, we do not expect the model to correctly follow one or the other core. The topography influences the amount of solar radiation received that in turn influences melting and wind erosion. At the same time, the topography modifies wind speed that in turn modifies topography itself. This results in a quasi random spatial variation and a systematic temporal variation in surface accumulation at a given location (Keck, 2001). Surface snow temperature was set equal to air temperature, instead of solving the full surface energy balance that would have required a higher availability of data; surface temperatures, in fact, may reach $0 \text{ }^\circ\text{C}$ also for air temperatures below $0 \text{ }^\circ\text{C}$ mainly when calm conditions are present or, on the contrary, melting may not occur during positive air temperatures particularly when wind is present (Keck, 2001).

From the box plots in Fig. 6 we observe that the conserved snow is made up mainly by summer precipitation and that the conserved fraction of solid precipitation reflects the number of hours with greater than zero temperature rather than the seasonality of precipitation. The accumulation is, in fact, mainly governed by the wind erosion (Wagenbach et al., 1988) and the presence of wet layers or ice crusts, as well as a faster compaction when temperatures are higher, protects snow from wind erosion. This is well known in ice core studies at CG, since it results in isotope records that are biased towards precipitation of the warm season (Schöner et al., 2002; Bohleber et al., 2013, 2018). To our knowledge, no models have been applied at CG that try to model the influence of wind speed and temperature on snow accumulation. The only confirmations of this behaviour we have, other than from ice core analysis, come from temporary measurements of the snow height in nearby sites or observations at CG. For example, at Seserjoch (Colle Sesia in Fig. 2), 4300 m a.s.l., the snow height was measured between 1998 and 2000 by Suter et al. (2001) and a main accumulation from about April to November, with practically no accumulation in high winter was observed. Assessing the link between temperature, wind speed and snow accumulation may be important under scenarios of climate warming for glacial sites, like CG, whose behaviour is strongly regulated by wind activity. At CG, our results suggest that higher temperatures may lead to a counterintuitive response in the snow mass balance, as already conjectured by Alean et al. (1983). In fact, an increase in melting due to a warmer climate may be compensated, or exceeded, by the consequent reduction in snow erosion, therefore resulting in a net snow accumulation increase.

5.3 Firm density

5.3.1 One-layer model version

465 The modelled densities have an opposite behaviour when compared with CG15 or KCC. In the first case, the average density is underestimated while in the second case overestimated. The multi-layer version of the model allows us to better understand the reasons of this mismatch. An error in the density of an individual layer will, in fact, affect all the modelled average firm densities that contain that individual layer. This is the case of CG15, where the underestimation of the density of the most superficial layers (Fig. 8) influences the average density of the whole firm column. This influence however decreases when
470 more annual layers are averaged. In the case of CG15, this is probably related with the characteristics of the CG15 location since underestimation was observed also when applying the firm densification model alone in steady-state and not inside the presented snow-firm model. On the contrary, the steady-state application of HL and AR resulted in a good match with KCC ice core (Fig. 4). Hence, it is reasonable to suppose that the mismatch is related with the modelled snow characteristics. This may be reconducted to the different estimated surface accumulations; the model, in fact, results in an average snow accumulation
475 of $0.46 \cdot 10^3 \text{ kg m}^{-2} \text{ y}^{-1}$ against the $0.22 \cdot 10^3 \text{ kg m}^{-2} \text{ y}^{-1}$ accumulation of KCC. Since the firm densification is driven by overburden stress, this may lead to a systematic bias in the results.

5.3.2 Multi-layer model version

Implementing HL inside the model, we obtained in general a better agreement and a higher variability in the density. The latter is probably related to a higher sensitivity of the equations to surface density, that has instead a low influence on AR as reported
480 also by Bréant et al. (2017). Choosing $\rho_D = 300 \text{ kg m}^{-3}$ and looking at KCC ice core, we observe a decrease in the density at around 7 – 8 m in both cores. This low density value corresponds to the layer deposited in the 2006–2007 hydrological year. This year was characterized by a solid precipitation event that occurred at the end of the hydrological year. As a consequence, the modelled average snow density decreased from 412 kg m^{-3} at the beginning of 25 September 2007 to 260.6 kg m^{-3} at the end of 27 September 2007. Due to the low amount of snow that is not eroded, new solid precipitation events, in fact, may have
485 a high influence on snow average density. The choice of adopting firm densification equations only after a certain density is reached rather than at the end of the water year allows to better model this circumstance, in which at the end of the water year the layer has characteristics that are more similar to recent snow rather than one year old snow. In comparing the observations and model results, it is also important to point out that, due to the differences in firm height between model and ice core, the age of the modelled and observed steps does not correspond.

490 The present model does not resolve a full energy balance to compute surface snow temperature, thus not taking into account the effect of the different amount of solar radiation in the different ice core locations, that is very likely responsible for the significantly different behaviours of the two ice cores. The ice core CG15 is closer to the axis saddle and presumably in a location with a higher exposition to solar radiation than KCC, since accumulation is doubled. Consequently, melting events may be more frequent in CG15 ice core. The differences in the model parameters when run for KCC or CG15 ice core are the
495 value of MAFT, ρ_D and γ' when AR is implemented and this limits the ability of the model to adapt to the different ice cores.

6 Conclusions

In this study we have proposed a local modelling that combines snow and firn dynamics. It was derived from the mass balance, momentum balance and rheological equations of snow and firn, combined with semi and empirical approaches proposed in literature to model the included mass fluxes. It requires in input a series of hourly (or sub-hourly) series of precipitation, temperature and wind speed with which the series of snow, water and ice inside the snowpack and firn height along with dry snow and firn density are computed. Two versions of the model were proposed: (1) a version (multi-layer) that considers separately each firn layer, and (2) a version (single-layer) that models firn and underlying glacier ice as a single layer. The two implementations allow to cover different purposes. A simpler model is, in fact, more suitable to reproduce firn inside a hydrological model, where the whole depth-density profile is not necessary and where a reduced number of equations may allow an easier integration. On the other hand, a model that resolves density with depth allows to assess the influence of meteorological variables on snow and firn characteristics. In order to obtain this, we integrated two existing firn densification models (other firn densification models could be possibly implemented) into a wider model, therefore moving the boundary of the model from surface accumulation and density to hourly meteorological series. While this may not be needed to retrieve past climatological information from ice cores, it is required to assess the response of the system under present and future changes in the climate.

Both the two model's versions require the calibration of three parameters a , e and γ' . In addition, also the parameters of the firn densification equation chosen may need calibration if applied to a temperate site. The modularity of the model allows to easily test different modelizations of the included fluxes. Depending also on the availability of measured data at the application site, less empirical approaches could be adopted for the mass fluxes. Also, depending on the specific application, some processes presented in the model may be neglected with a reduction in the total number of parameters. A high number of parameters are, for example, associated with wind effects that may be neglected in lower altitude sites, but that are likely to be important in high altitude sites (Haeberli and Alean, 1985). At Colle Gnifetti, for example, we saw that observed surface accumulations and densities cannot be explained if wind effects are not considered. The modelled reduction of annual snow accumulation due to wind erosion is on average $2 \cdot 10^3 \text{ kg m}^{-2} \text{ y}^{-1}$ while the increase in end of year snow density is on average 65 kg m^{-3} . The strong wind erosion results also in a greater correlation between the amount of snow preserved in each month and the number of days with above zero temperature rather than with the solid precipitation seasonality. This behaviour may be important in understanding the response of the site to a warming climate. All these elements result in a strong spatial and temporal variability in snow density and accumulation at CG, that is not captured by the model. This would, in fact, require to take in consideration the influence of topography on wind speed and the effect of solar radiation on surface snow temperature.

The aim of this study was to illustrate the new snow-firn modelling, and to present its potentiality through a case study. In order to integrate it into a hydrological model further steps are required, in particular fluxes among the different columns should be properly considered both regarding runoff and snow transport. In the present modelling, for example, we considered only the snow erosion. At CG the deposition can be neglected due to its characteristics. The site is a saddle with west-east orientation where the predominant wind direction coincides with the saddle orientation. Besides, an ice cliff at the end of it

530 works as a perfect sink for the eroded snow. A distributed modelling needs to take into account the presence of sink and source of snow transport. This will also improve the representation of wind effects on snow accumulation since, in order to include snow transport in a 1D framework, approximation of the process are unavoidable for the nature of the process itself.

Appendix A: Complete description and derivation of the snow-firn model

A1 Mass balance equations

535 The mass balance equations of snow (M_S), liquid water in snow (M_W), refrozen meltwater and rain in snow (M_{MF}), and firn (M_F) are as follows:

$$\frac{dM_S}{dt} = P_S - M - Q - E_S \quad (\text{A1a})$$

$$\frac{dM_W}{dt} = P_R + M + F - O - E_W \quad (\text{A1b})$$

$$\frac{dM_{MF}}{dt} = -F - E_{MF} \quad (\text{A1c})$$

540
$$\frac{dM_F}{dt} = -O_F + P_F + E_S + E_W + E_{MF} \quad (\text{A1d})$$

P_S and P_R are the mass of solid and liquid precipitation events and they are equal to $P_S = s \cdot \rho_{NS}$ and $P_R = r \cdot \rho_W$. The fresh snow density was calculated as proposed by Liston et al. (2007): $\rho_{NS} = \rho_{NS_0} + \rho_{NS_w}$. Following Anderson (1976), $\rho_{NS_0} = 50 \text{ kg m}^{-3}$ if the air temperature $T_A < -15^\circ\text{C}$ and $\rho_{NS_0} = 50 + 1.7 \cdot (T_A + 15)^{1.5} \text{ kg m}^{-3}$ otherwise. The second term gives the increase in fresh snow density due to wind and it is computed as $\rho_{NS_w} = D_1 + D_2(1.0 - \exp(-D_3(u_2 - 5)))$ where u_2 is the wind speed at 2 m height, $D_1 = 25 \text{ kg m}^{-3}$, $D_2 = 250.0 \text{ kg m}^{-3}$ and $D_3 = 0.2 \text{ s m}^{-1}$. When $u_2 \leq 5 \text{ m s}^{-1}$, $\rho_{NS_w} = 0 \text{ kg m}^{-3}$.

M is the snow melt mass flux that was computed with a temperature-index approach (Hock, 2003): $M = (I \cdot a)(T_A - T_\tau)\rho_S$.

F is the melt freeze mass flux that was modelled with a coupled melt-freeze temperature-index approach: $F = (I^* \cdot e \cdot a)(T_A - T_\tau)\rho_W$.

550 The run-off O was modelled with a matrix flow approach and it is equal to $O = \rho_W \alpha K_W$ where $\alpha = \alpha'(5.47 \cdot 10^5 \text{ m}^{-1} \text{ s}^{-1})$ (DeWalle and Rango, 2008) with $\alpha' = 3600 \text{ s h}^{-1}$. Following Colbeck (1972), K_W was computed as $K_W = K S^*$ in which K is the intrinsic permeability of snow in m^2 and S^* is the effective saturation degree of the mixture equal to $S^* = (S_r - S_{r_i})/(1 - S_{r_i})$ where S_{r_i} is the irreducible saturation degree equal to $S_{r_i} = 0.02\rho_S/(\rho_W\phi)$ (Kelleners et al., 2009) and S_r is the average saturation degree of the porous matrix equal to 1 when $h_W \geq \phi h_S$ while $S_r = h_W/(\phi h_S)$ otherwise (Avanzi et al., 2015). The intrinsic permeability is obtained using the parametrization proposed by Calonne et al. (2012) and it is equal to $K = 3R^2 \exp(-0.013\rho_S)$ in which R is the equivalent sphere radius. The radius R is defined as $R = 3/(SSA\rho_i)$ where SSA is the specific surface area in $\text{m}^2 \text{ kg}^{-1}$ that was computed by Avanzi et al. (2015) adapting the formula proposed by Domine et al. (2007) for which $SSA = -30.82 \ln(\rho_S \cdot 10^{-3}) - 20.60$. When $S_r > 0.5$, to avoid numerical instability, the run-off was calculated with a kinematic wave approximation (De Michele et al., 2013) as $\rho_W \theta_W h_W^{1.25}$.

560 The firm melting O_F , that may occur only when the snowpack is absent, was modelled with a temperature-index approach and it is equal to $O_F = (I_F \cdot a)(T_A - T_\tau)\rho_F\delta(h_S)$.

P_F is the effect of rain on firm that, when the snowpack is absent, causes an increase of M_F when $T_A < 0^\circ\text{C}$ because rainfall is chilled to the firm temperature and a decrease when $T_A > 0^\circ\text{C}$ because the energy supplied by rain will be used to melt ice. In the first case $P_F = \rho_W \cdot r$ while in the second case P_F was set to zero due to its small contribution to mass balance (Doyle
565 et al., 2015).

The terms E_S , E_W , E_{MF} move the mass of the snowpack still on the ground at the end of each melt season inside the firm and they are equal to $E_j = \sum_i \rho_j \frac{h_j}{dt} \delta(t - t_i)$ with $j = S, MF, W$.

Q is the mass of snow eroded by wind obtained from snow transport. The latter was computed adopting the parametrization proposed by Pomeroy et al. (1993) as the sum of a transport in saltation and a transport in suspension.

570 The saltation transport rate Q_{salt} ($\text{kg m}^{-1} \text{s}^{-1}$) occurs only when wind exceeds a given threshold and it is computed as follows:

$$Q_{salt} = \frac{0.68\rho_a u_t^*}{u^* g} (u^{*2} - u_t^{*2}) \quad (\text{A2})$$

where ρ_a is the atmospheric density (kg m^{-3}) and u^* and u_t^* are respectively the atmospheric friction velocity and the friction velocity applied to the snow surface at the transport threshold (m s^{-1}). To move from the measured wind speed u to u^* ,
575 knowledge of the aerodynamic roughness height z_0 is required. This passage is not straightforward since the value of z_0 during blowing snow events is different from the one during non transport conditions and it depends on friction velocity (Pomeroy and Gray, 1990). In order to avoid an iterative procedure, we adopted the approximation proposed by Pomeroy and Gray (1990) setting $u^* \approx 0.02264u^{1.295}$ and $z_0 = \frac{0.1203u^{*2}}{2g}$ where u is 10 m wind speed (m s^{-1}).

Suspension transport, that occurs only when particles are already in saltation, was computed as follows:

$$580 \quad Q_{susp} = \frac{u^*}{\kappa} \int_{h^*}^{z_b} \eta(z) \ln\left(\frac{z}{z_0}\right) dz \quad (\text{A3})$$

where Q_{susp} is in $\text{kg m}^{-1} \text{s}^{-1}$, κ is the von Kármán constant equal to 0.4, h^* is the lower boundary for suspension equal to $h^* = c_H u^{*1.27}$ (Pomeroy and Male, 1992) with $c_H = 0.08436 \text{ m}^{-0.27} \text{ s}^{1.27}$, z_b is the top of the surface boundary-layer for suspended snow and $\eta(z)$ is the mass concentration of suspended snow (kg m^{-3}) at height z . The mass concentration can be approximate as $\eta(z) = \eta(z_r) \exp(-A_Q((B_Q u^*)^{-0.544} - z^{-0.544}))$ (Pomeroy and Male, 1992) where $\eta(z_r)$ is the reference
585 mass concentration for suspension set to 0.8 kg m^{-3} (Pomeroy and Male, 1992), A_Q is equal to $1.55 \text{ m}^{0.544}$ and B_Q to $0.05628 \text{ s}^{-0.544}$. z_b was set to 5 m, since its value is typically between 5 m and 10 m (Déry and Taylor, 1996). The exact value is unimportant because of small mass fluxes at this height (Pomeroy et al., 1993). The snow erosion in the control volume of the model was set equal to the sum of these two transports.

The critical threshold, above which snow transport occurs, was computed adopting the formula proposed by He and Ohara
590 (2017). The critical shear stress for snow movement can be therefore computed as:

$$\tau_t = \frac{(8R \cdot C_g \cdot g)(\rho_S - \rho_a) \cos(\pi/3 - S) + (\pi C_{cs}) \left(\frac{C}{R^m} t_d\right)^{2/n} \left(\sin(\pi/3 + S) + \left(\frac{C}{R^m} t_d\right)^{1/n}\right)}{2(C_d \sin(\pi/3 - S) + C_l \cos(\pi/3 - S))} \quad (\text{A4})$$

where R is the grain radius (m), t_d is the time since deposition in seconds, C_c , C_d , C_g and C_l are dimensionless coefficients set to 1, 4, $1.3\pi/6$ and 3.4 (He and Ohara, 2017), ς is the stress caused by cohesion of ice computed as $\varsigma = 1.51 \exp(0.44(T_A + 9)) + 6.8$ (Hosler et al., 1957) for temperatures between -20 °C and 0 °C with ς in N m^{-2} and T_A in
595 °C and $S = \arcsin\left(\left(\frac{C}{R^m} t_d\right)^{1/n}\right)$. C , m and n are parameters that influence the rate of ice sintering, modelled following Maeno and Arakawa (2004). In particular, $C = C_0 \exp\left(\frac{-Q_s}{R_G(T_A + 273.15)}\right)$ in which R_G is the gas constant and T_A is computed as the average air temperature since deposition, $C_0 = 4.14 \cdot 10^{19} \text{ m}^3 \text{ s}^{-1}$ and $Q_s = 1.965 \cdot 10^5 \text{ J mol}^{-1}$. Finally, m and n are empirical parameters set to 2.9 and 5 respectively following the results of He and Ohara (2017). Once the critical shear stress is obtained it is possible to move to critical friction velocity as follows: $u_t^* = \sqrt{\tau_t / \rho_a}$. If wind speed is lower than the critical
600 threshold, no erosion occurs and Q is set to zero.

To implement the snow erosion routine, we proceeded as explained in the following. When the first solid precipitation event occurs in a time step, the amount of new snow on the ground at the end of the time step, S_A ($\text{kg m}^{-2} \text{ h}^{-1}$), is saved along with the time of deposition and ρ_{NS} of the event. During the following step four different situations are possible: (1) a new snow event occurs in the time step. In this case S_A is moved into a vector \mathbf{S}_R with its time of deposition and ρ_{NS} . S_A is recomputed
605 as $\rho_{NS} \cdot s$; (2) $T_A > 0$ °C. In this case S_A and Q are set to $0 \text{ kg m}^{-2} \text{ h}^{-1}$ and all the old snow events memorized in \mathbf{S}_R are removed; (3) $T_A < 0$ °C and $Q < S_A$. In this case S_A is set to $S_A = S_A - Q$; (4) $T_A < 0$ °C and $Q > S_A$. In this case, if \mathbf{S}_R has no elements, Q is set equal to S_A and S_A to $0 \text{ kg m}^{-2} \text{ h}^{-1}$, otherwise the difference between Q and S_A is subtracted from the most recent event in \mathbf{S}_R , given that wind speed is higher than the threshold recomputed with the characteristics of that event, and this event is removed from \mathbf{S}_R . This is repeated until an event in \mathbf{S}_R that cannot be eroded by wind is encountered
610 or the total amount of snow eroded in that time step reaches Q . In the latter case the actual transport is Q while in the former Q is given by the total amount of snow eroded before reaching the non erodible layer. The new S_A is the amount of snow associated with the last event considered.

Given that $M_j = \rho_j h_j$ and $\rho_k = \text{const}$ with $j = S, MF, W$ and $k = MF, W$, after some algebra we can move from Eqs. A1a–A1d to Eqs. 2a–2d.

615 A2 Snow densification

The densification of dry snow due to compaction was modelled adopting the formula proposed by Liston et al. (2007):

$$\frac{d\rho_S}{dt} = (c \cdot A_1 \cdot U) \rho_S \exp(-B \cdot (T_\tau - T_S) - A_2 \cdot \rho_S) \quad (\text{A5})$$

where $c = 0.10 \cdot 3600 \text{ s h}^{-1}$, $A_1 = 0.0013 \text{ m}^{-1}$, $A_2 = 0.021 \text{ m}^3 \text{ kg}^{-1}$, $B = 0.08 \text{ K}^{-1}$ and U is the wind speed contribution (m s^{-1}). For wind speeds $\geq 5 \text{ m s}^{-1}$, $U = E_1 + E_2(1.0 - \exp(-E_3(u_2 - 5.0)))$ with E_1 , E_2 and E_3 equal to 5.0 m s^{-1} ,
620 15.0 m s^{-1} and 0.2 s m^{-1} , respectively, and u_2 the wind speed at 2 m height. For wind speed $< 5 \text{ m s}^{-1}$, $U = 1 \text{ m s}^{-1}$. Adding the densification due to mass variation (see De Michele et al. (2013)) the total densification rate can be computed as follows:

$$\frac{d\rho_S}{dt} = (c \cdot A_1 \cdot U) \rho_S \exp(-B \cdot (T_\tau - T_S) - A_2 \cdot \rho_S) + \frac{\rho_{NS} - \rho_S}{h_S} s \quad (\text{A6})$$

where we assumed that melting events and snow erosion occur at $\rho_S = \text{const}$.

A3 Arnaud et al. (2000) model

625 The model of AR separates the densification of firm into three stages. The first stage is governed by settling and it is modelled
 by Bréant et al. (2017) adapting the equation proposed by Alley (1987). The second stage, that starts when the relative density
 $D = \rho_F / \rho_i$ equals D_0 , is dominated by power law creep and it is modelled following Arzt (1982) and Arzt et al. (1983). Grains
 are considered as spheres and each sphere is allowed to increase in radius around fixed centres. Starting from an initial radius
 l , the new radius l' (in units of the initial particle radius l) is $l'(D) = (D/D_0)^{1/3}$. The growth of spheres increases the number
 630 of particle contacts Z from the initial value Z_0 to $Z(D) = Z_0 + b(l' - 1)$ in which $b = 15.5$. The overlap due to the growth of
 particles produces an excess volume of material. This excess is distributed uniformly around the portion of the surface of the
 spheres not in contact. From this excess volume, it is possible to calculate the new radius l'' as

$$l'' = l' + \frac{4Z_0(l' - 1)^2(2l' + 1) + b(l' - 1)^3(3l' + 1)}{12l'(4l' - 2Z_0(l' - 1) - b(l' - 1)^2)} \quad (\text{A7})$$

The average contact area (in unit of l^2) can be obtained averaging over all of existing contacts:

$$635 \quad a_c(D) = a_c(l'') = \frac{\pi}{3Zl'^2} (3(l''^2 - 1)Z_0 + l''^2 b(2l'' - 3) + b) \quad (\text{A8})$$

The value of Z_0 for a given value of D_0 is obtained, as proposed by Arnaud et al. (2000), assuming that the effective stress
 $P^* = (4\pi P)/(a_c Z D)$ approaches P as D tends to 1. The third stage begins when pores start becoming isolated ($D > D_c$)
 and densification is calculated considering the deformation of ice shells surrounding cylindrical pores (Wilkinson and Ashby,
 1975). As for Eq. 2e, the total densification rate is obtained adding the densification due to new mass addition (Eq. 2f).

640 Appendix B: List of all the symbols used

Table B1. List of the symbols used in the mass fluxes of the snow-firn model with the exclusion of snow erosion (from A to S).

Symbol	Description	Type	Unit
a	degree hour parameter	calibration parameter	$\text{m h}^{-1} \text{ } ^\circ\text{C}^{-1}$
D_1, D_2	constants governing the influence of wind in fresh snow density	constant	kg m^{-3}
D_3	constants governing the influence of wind in fresh snow density	constant	$\text{m}^{-1} \text{ s}$
E_{MF}, E_S, E_W	mass flux due to the transformation of snow in firn	variable	$\text{kg m}^{-2} \text{ h}^{-1}$
e	melt-freeze factor	calibration parameter	–
F	melt freeze mass flux	variable	$\text{kg m}^{-2} \text{ h}^{-1}$
h	snowpack height	variable	m
h_F	firn height	variable	m
h_{MF}	height of ice inside the snowpack	variable	m
h_S	dry snow height	variable	m
h_W	height of water inside the snowpack	variable	m
I, I^*, I_F	multiplicative function	function	
K	intrinsic permeability of snow	variable	m^2
K_W	intrinsic permeability of water in snow	variable	m^2
k	constant	constant	m
M	snow melt mass flux	variable	$\text{kg m}^{-2} \text{ h}^{-1}$
M_F	firn mass	variable	kg m^{-2}
M_{MF}	mass of ice inside the snowpack	variable	kg m^{-2}
M_S	dry snow mass	variable	kg m^{-2}
M_W	mass of water inside the snowpack	variable	kg m^{-2}
O	run-off rate	variable	$\text{kg m}^{-2} \text{ h}^{-1}$
O_F	firn melt mass flux	variable	$\text{kg m}^{-2} \text{ h}^{-1}$
P_F	variation of mass due to rain on firn	variable	$\text{kg m}^{-2} \text{ h}^{-1}$
P_R	mass flux of liquid precipitation	variable	$\text{kg m}^{-2} \text{ h}^{-1}$
P_S	mass flux of solid precipitation	variable	$\text{kg m}^{-2} \text{ h}^{-1}$
R	grain radius	variable	m
r	liquid precipitation rate	variable	m h^{-1}
S^*	effective saturation degree of the snowpack	variable	–
S_r	average saturation degree of the porous matrix	variable	–
S_{r_i}	irreducible saturation degree	variable	–
s	solid precipitation rate	variable	m h^{-1}
SSA	specific surface area	variable	$\text{m}^2 \text{ kg}^{-1}$
SWE	snow water equivalent	variable	m

Table B2. List of the symbols used in the mass fluxes of the snow-firn model with the exclusion of snow erosion (from T to Z and Greek letters).

Symbol	Description	Type	Unit
T_A	air temperature	variable	$^{\circ}\text{C}$
T_{τ}	threshold temperature for melting	here treated as constant	$^{\circ}\text{C}$
u_2	2 m wind speed	variable	m s^{-1}
V_F	firn volume	variable	m^3
V_{MF}	volume of ice inside the snowpack	variable	m^3
V_S	dry snow volume	variable	m^3
V_W	volume of water inside the snowpack	variable	m^3
α	constant governing run-off rate	constant	$\text{m}^{-1} \text{s}^{-1}$
α'	time conversion constant	constant	s h^{-1}
ρ	bulk density of snow	variable	kg m^{-3}
ρ_F	firn density	variable	kg m^{-3}
ρ_i	ice density	here treated as constant	kg m^{-3}
ρ_{NS}	fresh snow density	variable	kg m^{-3}
ρ_{NS_0}	fresh snow density without wind	variable	kg m^{-3}
ρ_{NS_w}	fresh snow density increase due to wind	variable	kg m^{-3}
ρ_S	dry snow density	variable	kg m^{-3}
ρ_W	water density	here treated as constant	kg m^{-3}
θ_W	volumetric liquid water content	variable	–
ϕ	porosity	variable	–

Table B3. List of the symbols used to compute snow erosion.

Symbol	Description	Type	Unit
A_Q	constant governing the mass concentration of suspended snow	constant	$m^{0.544}$
B_Q	constant governing the mass concentration of suspended snow	constant	$s^{-0.544}$
C	constant governing ice sintering function of T_A	constant	$m^3 s^{-1}$
C_0	constant governing ice sintering	constant	$m^3 s^{-1}$
C_c, C_d, C_g, C_l	coefficient governing cohesive force, drag, form and lift coefficient	parameter	–
c_H	coefficient influencing the lower boundary height for suspension	constant	$m^{-0.27} s^{1.27}$
g	gravitational acceleration	constant	$m s^{-2}$
h^*	lower boundary for suspension	variable	m
m	parameter governing ice sintering	parameter	–
n	parameter governing ice sintering	parameter	–
Q	snow erosion	variable	$kg m^{-2} h^{-1}$
Q_s	activation energy	constant	$J mol^{-1}$
Q_{salt}	snow transport in saltation	variable	$kg m^{-1} s^{-1}$
Q_{susp}	snow transport in saltation	variable	$kg m^{-1} s^{-1}$
R	grain radius	variable	m
R_G	gas constant	constant	$J K^{-1} mol^{-1}$
S_A	mass of the most recent non eroded snow events	variable	$kg m^{-2} h^{-1}$
\mathbf{S}_R	vector of non eroded snow events	variable	$kg m^{-2} h^{-1}$
t_d	time since deposition	variable	s
u	10 m wind speed	variable	$m s^{-1}$
u^*	atmospheric friction velocity	variable	$m s^{-1}$
u_t^*	critical friction velocity	variable	$m s^{-1}$
z	altitude	variable	m
z_0	aerodynamic roughness length	variable	m
z_b	top boundary for suspension	here treated as constant	m
z_r	reference height for mass concentration of suspended snow	constant	m
η	mass concentration of suspended snow	variable	$kg m^{-3}$
κ	von Kármán constant	constant	–
ρ_a	atmospheric density	here treated as constant	$kg m^{-3}$
ρ_s	dry snow density	variable	$kg m^{-3}$
ς	stress due to ice cohesion	variable	Pa
τ_t	critical shear stress for erosion	variable	Pa

Table B4. List of the symbols used in AR.

Symbol	Description	Type	Unit
A	creep constant function of T_F	constant	$\text{Pa}^{-3} \text{h}^{-1}$
A_0	constant governing firn densification	constant	$\text{Pa}^{-3} \text{h}^{-1}$
a_c	average contact area	variable	—
b	parameter in firn densification	parameter	—
D	relative firn density	variable	—
D_0	relative density between first and second stage of firn densification	here treated as constant	—
D_c	close-off density	here treated as constant	—
D_D	relative surface density	variable	—
l', l''	firn grain radius in units of the initial radius l	variable	—
P	overburden pressure	variable	Pa
P^*	effective stress	variable	Pa
P_b	pressure in the bubbles	variable	Pa
P_c	atmospheric pressure at the close-off	here treated as constant	Pa
Q_1, Q_2	activation energy	constant	J mol^{-1}
R_G	gas constant	constant	$\text{J K}^{-1} \text{mol}^{-1}$
T_F	average firn temperature	variable	$^{\circ}\text{C}$
Z	number of particle contacts	variable	—
Z_0	initial number of particle contacts	constant	—
γ	parameter function of γ', T_F	parameter	$\text{Pa}^{-1} \text{h}^{-1}$
γ'	parameter governing firn densification	calibration parameter	$\text{Pa}^{-1} \text{h}^{-1}$
ρ_F	firn density	variable	kg m^{-3}
ρ_i	ice density	here treated as constant	kg m^{-3}

Table B5. List of the symbols used in HL.

Symbol	Description	Type	Unit
k_0	constant governing firn densification	constant	m^{-1}
k_1	constant governing firn densification	constant	$\text{m}^{-0.5} \text{y}^{-0.5}$
R_G	gas constant	constant	$\text{J K}^{-1} \text{mol}^{-1}$
T_F	average firn temperature	variable	$^{\circ}\text{C}$
ρ_D	surface density	variable	kg m^{-3}
ρ_F	firn density	variable	kg m^{-3}
ρ_i	ice density	here treated as constant	kg m^{-3}
ω	mean annual accumulation	variable	$\text{kg m}^{-2} \text{y}^{-1}$

Table B6. List of the symbols related to snow densification rate.

Symbol	Description	Type	Unit
A_1	constant governing snow densification	constant	m^{-1}
A_2	constant governing snow densification	constant	$\text{m}^3 \text{kg}^{-1}$
B	constant governing snow densification	constant	K^{-1}
c	constant governing snow densification	constant	s h^{-1}
E_1, E_2	constants governing the influence of wind in snow densification	constant	m s^{-1}
E_3	constants governing the influence of wind in snow densification	constant	$\text{m}^{-1} \text{s}$
T_S	average snow temperature	variable	$^{\circ}\text{C}$
T_τ	threshold temperature for melting	here treated as constant	$^{\circ}\text{C}$
U	wind speed contribution to snow densification	variable	m s^{-1}
u_2	2 m wind speed	variable	m s^{-1}
ρ_S	dry snow density	variable	kg m^{-3}

Table B7. List of other symbols used throughout the paper.

Symbol	Description	Type	Unit
H	mountain height	constant	m
$MAAT$	mean annual air temperature	constant	$^{\circ}\text{C}$
$MAFT$	mean annual firn temperature	constant	$^{\circ}\text{C}$
p	daily precipitation	variable	mm d^{-1}
SD	observed snow depth	variable	m
T_0	surface temperature	variable	$^{\circ}\text{C}$
T_A	air temperature	variable	$^{\circ}\text{C}$
t_i	time instant at the end of hydrological year i	constant	h
u	10 m wind speed	variable	m s^{-1}
z_M	maximum firn depth influenced by air temperature	here treated as constant	m
z_m	altitude of maximum precipitation	here treated as constant	m
Δt	time step	constant	h
δ	Dirac delta function	function	

Author contributions. CDM and FB conceived the model. FB took care of data, and developed the case study. FB wrote a first draft of the manuscript. FB and CDM reviewed the manuscript.

Competing interests. No competing interests are present.

Acknowledgements. We would like to thank ARPA Piemonte for the meteorological data used in this study, with particular thanks to Manuela Bassi, and Aosta Valley for the snow water equivalent data. Gratitude is also due to Carlo Licciulli and Josef Lier for ice core data and to Pascal Bohleber for the information about Colle Gnifetti. One last thank you to Scenari Digitali and Rifugi Monterosa for additional information about Capanna Regina Margherita.

References

- Adhikary, S. P.: Inaugural address, in: Snow and glacier hydrology, edited by Young, G. J., p. x, International Association of Hydrological Sciences (IAHS), Wallingford, Oxfordshire OX10 8BB, UK., 1993.
- 650 Aizen, V. B., Aizen, E. M., and Melack, J. M.: Precipitation, melt and runoff in the northern Tien Shan, *J. Hydrol.*, 186, 229–251, [https://doi.org/10.1016/S0022-1694\(96\)03022-3](https://doi.org/10.1016/S0022-1694(96)03022-3), 1996.
- Alean, J., Haeberli, W., and Schädler, B.: Snow accumulation, firn temperature and solar radiation in the area of the Colle Gnifetti core drilling site (Monte Rosa, Swiss Alps): distribution patterns and interrelationships, *Zeitschrift für Gletscherkunde und Glazialgeologie*, 655 19, 131–147, 1983.
- Alley, R. B.: Firn densification by grain-boundary sliding: a first model, *J. Phys. Colloques*, 48, C1–249–C1–256, <https://doi.org/10.1051/jphyscol:1987135>, 1987.
- Alpert, P.: Mesoscale Indexing of the Distribution of Orographic Precipitation over High Mountains, *J. Climate Appl. Meteor.*, 25, 532–545, [https://doi.org/10.1175/1520-0450\(1986\)025<0532:MIOTDO>2.0.CO;2](https://doi.org/10.1175/1520-0450(1986)025<0532:MIOTDO>2.0.CO;2), 1986.
- 660 Anderson, E. A.: A point energy and mass balance model of a snow cover, vol. 19, NOAA Technical Report NWS, 1976.
- Ardenghi, N.: Geochemical characterization of a shallow firn core retrieved from Colle Gnifetti (Monte Rosa, Italy), Master's thesis, Università Ca' Foscari Venezia, Italy, 2012.
- Arnaud, L., Barnola, J. M., and Duval, P.: Physical modeling of the densification of snow/firn and ice in the upper part of polar ice sheets, in: *Physics of ice core records*, edited by Hondoh, T., pp. 285–305, Hokkaido University Press, Sapporo, Japan, 2000., 2000.
- 665 Arthern, R. J., Vaughan, D. G., Rankin, A. M., Mulvaney, R., and Thomas, E. R.: In situ measurements of Antarctic snow compaction compared with predictions of models, *J. Geophys. Res.-Earth*, 115, <https://doi.org/10.1029/2009JF001306>, 2010.
- Arzt, E.: The influence of an increasing particle coordination on the densification of spherical powders, *Acta Metall. Mater.*, 30, 1883–1890, [https://doi.org/10.1016/0001-6160\(82\)90028-1](https://doi.org/10.1016/0001-6160(82)90028-1), 1982.
- Arzt, E., Ashby, M. F., and Easterling, K. E.: Practical applications of hotisostatic pressing diagrams: four case studies, *Metall. Mater. Trans.* 670 A, 14, 211–221, <https://doi.org/10.1007/BF02651618>, 1983.
- Avanzi, F., De Michele, C., Ghezzi, A., Jommi, C., and Pepe, M.: A processing- modeling routine to use SNOTEL hourly data in snowpack dynamic models, *Adv. Water Resour.*, 73, 16–29, <https://doi.org/10.1016/j.advwatres.2014.06.011>, 2014.
- Avanzi, F., Yamaguchi, S., Hirashima, H., and De Michele, C.: Bulk volumetric liquid water content in a seasonal snowpack: modeling its dynamics in different climatic conditions, *Adv. Water Resour.*, 86, 1–13, <https://doi.org/10.1016/j.advwatres.2015.09.021>, 2015.
- 675 Bader, H.: Sorge's Law of densification of snow on high polar glaciers, *J. Glaciol.*, 2, 319–323, <https://doi.org/10.3189/S0022143000025144>, 1954.
- Bainov, D. and Simeonov, P.: *Impulsive differential equations: periodic solutions and applications*, vol. 66, Longman, England, 1993.
- Benn, D. I. and Evans, D. J. A.: *Glaciers and glaciation (Second edition)*, Hodder Education, London, 2010.
- Bohleber, P., Wagenbach, D., Schöner, W., and Böhm, R.: To what extent do water isotope records from low accumulation Alpine ice cores reproduce instrumental temperature series?, *Tellus B*, 65, 20 148, <https://doi.org/10.3402/tellusb.v65i0.20148>, 2013.
- 680 Bohleber, P., Erhardt, T., Spaulding, N., Hoffmann, H., Fischer, H., and Mayewski, P.: Temperature and mineral dust variability recorded in two low-accumulation Alpine ice cores over the last millennium, *Clim. Past*, 14, 21–37, <https://doi.org/10.5194/cp-14-21-2018>, 2018.
- Bréant, C., Martinerie, P., Orsi, A., Arnaud, L., and Landais, A.: Modelling firn thickness evolution during the last deglaciation: constraints on sensitivity to temperature and impurities, *Clim. Past*, 13, 833–853, <https://doi.org/10.5194/cp-13-833-2017>, 2017.

- 685 Calonne, N., Geindreau, C., Flin, F., Morin, S., Lesaffre, B., Rolland Du Roscoat, S., and Charrier, P.: 3-D image-based numerical computations of snow permeability: links to specific surface area, density, and microstructural anisotropy, *Cryosphere*, 6, 939–951, <https://doi.org/10.5194/tc-6-939-2012>, 2012.
- Colbeck, S.: A theory of water percolation in snow, *Journal of glaciology*, 11, 369–385, <https://doi.org/10.3189/S0022143000022346>, 1972.
- Cuffey, K. M. and Paterson, W. S. B.: *The physics of glaciers* (Fourth edition), Butterworth Heinemann-Elsevier, Burlington, 2010.
- 690 De Michele, C., Avanzi, F., Ghezzi, A., and Jommi, C.: Investigating the dynamics of bulk snow density in dry and wet conditions using a one-dimensional model, *Cryosphere*, 7, 433–444, <https://doi.org/10.5194/tc-7-433-2013>, 2013.
- Déry, S. J. and Taylor, P. A.: Some aspects of the interaction of blowing snow with the atmospheric boundary layer, *Hydrol. Process.*, 10, 1345–1358, [https://doi.org/10.1002/\(SICI\)1099-1085\(199610\)10:10<1345::AID-HYP465>3.0.CO;2-2](https://doi.org/10.1002/(SICI)1099-1085(199610)10:10<1345::AID-HYP465>3.0.CO;2-2), 1996.
- DeWalle, D. R. and Rango, A.: *Principles of snow hydrology*, Cambridge University Press, New York, 2008.
- 695 Domine, F., Taillandier, A.-S., and Simpson, W. R.: A parameterization of the specific surface area of seasonal snow for field use and for models of snowpack evolution, *J. Geophys. Res.-Earth*, 112, <https://doi.org/10.1029/2006JF000512>, 2007.
- Doyle, S. H., Hubbard, A., Van De Wal, R. S., Box, J. E., Van As, D., Scharrer, K., Meierbachtol, T. W., Smeets, P. C., Harper, J. T., and Johansson, E.: Amplified melt and flow of the Greenland ice sheet driven by late-summer cyclonic rainfall, *Nat. Geosci.*, 8, 647–653, <https://doi.org/10.1038/ngeo2482>, 2015.
- 700 Duan, Q., Sorooshian, S., and Gupta, V.: Effective and efficient global optimization for conceptual rainfall-runoff models, *Water Resour. Res.*, 28, 1015–1031, <https://doi.org/10.1029/91WR02985>, 1992.
- Duan, Q. Y., Gupta, V. K., and Sorooshian, S.: Shuffled complex evolution approach for effective and efficient global minimization, *J. of Optimiz. Theory App.*, 76, 501–521, <https://doi.org/10.1007/BF00939380>, 1993.
- Eichler, A., Schwikowski, M., Gäggeler, H. W., Furrer, V., Synal, H.-A., Beer, J., Saurer, M., and Funk, M.: Glaciochemical dating of an ice core from upper Grenzgletscher (4200 m a.s.l.), *J. Glaciol.*, 46, 507–515, <https://doi.org/10.3189/172756500781833098>, 2000.
- 705 Fountain, A. G. and Tangborn, W. V.: The Effect of Glaciers on Streamflow Variations, *Water Resour. Res.*, 21, 579–586, <https://doi.org/10.1029/WR021i004p00579>, 1985.
- Gäggeler, H., von Gunten, H. R., Rössler, E., Oeschger, H., and Schotterer, U.: 210 Pb dating of Cold Alpine Firm/Ice Cores From Colle Gnifetti, Switzerland, *J. Glaciol.*, 29, 165–177, <https://doi.org/10.3189/2014AoG66A151>, 1983.
- 710 Haerberli, W. and Alean, J.: Temperature and accumulation of high altitude firn in the Alps, *Ann. Glaciol.*, 6, 161–163, <https://doi.org/10.3189/1985AoG6-1-161-163>, 1985.
- Haerberli, W. and Funk, M.: Borehole temperatures at the Colle Gnifetti core-drilling site (Monte Rosa, Swiss Alps), *J. Glaciol.*, 37, 37–46, <https://doi.org/10.3189/S0022143000042775>, 1991.
- Hagg, W., Braun, L. N., Kuhn, M., and Nesgaard, T. I.: Modelling of hydrological response to climate change in glacierized Central Asian catchments, *J. Hydrol.*, 332, 40–53, <https://doi.org/10.1016/j.jhydrol.2006.06.021>, 2007.
- 715 He, S. and Ohara, N.: A New Formula for Estimating the Threshold Wind Speed for Snow Movement, *J. Adv. Model. Earth Sy.*, 9, 2514–2525, <https://doi.org/10.1002/2017MS000982>, 2017.
- Henn, B., Raleigh, M. S., Fisher, A., and Lundquist, J. D.: A comparison of methods for filling gaps in hourly near-surface air temperature data, *J. Hydrometeorol.*, 14, 929–945, <https://doi.org/10.1175/JHM-D-12-027.1>, 2013.
- 720 Herron, M. M. and Langway, C. C.: Firn Densification: An Empirical Model, *J. Glaciol.*, 25, 373–385, <https://doi.org/10.1017/S0022143000015239>, 1980.

- Hock, R.: Temperature index melt modelling in mountain areas, *J. Hydrol.*, 282, 104–115, [https://doi.org/10.1016/S0022-1694\(03\)00257-9](https://doi.org/10.1016/S0022-1694(03)00257-9), 2003.
- 725 Hock, R., Jansson, P., and Braun, L. N.: Modelling the response of mountain glacier discharge to climate warming, in: *Global Change and Mountain Regions*, edited by Huber, U., Bugmann, H., and M.A., R., vol. 23 of *Advances in Global Change Research*, pp. 243–252, Springer, Dordrecht, 2005.
- Hock, R., Rasul, G., Adler, C., Cáceres, B., Gruber, S., Hirabayashi, Y., Jackson, M., Käab, A., Kang, S., Kutuzov, S., Milner, A., Molau, U., Morin, S., Orlove, B., and Steltzer, H.: High Mountain Areas, in: *IPCC Special Report on the Ocean and Cryosphere in a Changing Climate*, edited by Pörtner, H.-O., Roberts, D. C., Masson-Delmotte, V., Zhai, P., Tignor, M., Poloczanska, E., Mintenbeck, K., Alegría, A., Nicolai, M., Okem, A., Petzold, J., Rama, B., and Weyer, N. M., In press, 2019.
- 730 Hosler, C. L., Jensen, D. C., and Goldshlak, L.: On the aggregation of ice crystals to form snow, *J. Meteor.*, 14, 415–420, [https://doi.org/10.1175/1520-0469\(1957\)014<0415:OTAOIC>2.0.CO;2](https://doi.org/10.1175/1520-0469(1957)014<0415:OTAOIC>2.0.CO;2), 1957.
- Huss, M.: Density assumptions for converting geodetic glacier volume change to mass change, *Cryosphere*, 7, 877–887, <https://doi.org/10.5194/tc-7-877-2013>, 2013.
- 735 Huss, M., Juvet, G., Farinotti, D., and Bauder, A.: Future high-mountain hydrology: a new parameterization of glacier retreat, *Hydrol. Earth Syst. Sc.*, 14, 815–829, <https://doi.org/10.5194/hess-14-815-2010>, 2010.
- Hyndman, R. J. and Athanasopoulos, G.: *Forecasting: principles and practice*, OTexts, 2018.
- Jacka, T. and Jun, L.: The steady-state crystal size of deforming ice, *Ann. Glaciol.*, 20, 13–18, <https://doi.org/10.3189/1994AoG20-1-13-18>, 1994.
- 740 Jansson, P., Hock, R., and Schneider, T.: The concept of glacier storage: a review, *J. Hydrol.*, 282, 116–129, [https://doi.org/10.1016/S0022-1694\(03\)00258-0](https://doi.org/10.1016/S0022-1694(03)00258-0), 2003.
- Jennings, K. S., Winchell, T. S., Livneh, B., and Molotch, N. P.: Spatial variation of the rain-snow temperature threshold across the Northern Hemisphere, *Nat. Commun.*, 9, 1148, <https://doi.org/10.1038/s41467-018-03629-7>, 2018.
- Jost, G., Moore, R. D., Menounos, B., and Wheate, R.: Quantifying the contribution of glacier runoff to streamflow in the upper Columbia River Basin, Canada, *Hydrol. Earth Syst. Sc.*, 16, 849–860, <https://doi.org/10.5194/hess-16-849-2012>, 2012.
- 745 Keck, L.: Climate significance of stable isotope records from Alpine ice cores, Ph.D. thesis, Institute of Environmental Physics, Heidelberg University, Germany, 2001.
- Kelleners, T., Chandler, D., McNamara, J. P., Gribb, M. M., and Seyfried, M.: Modeling the water and energy balance of vegetated areas with snow accumulation, *Vadose Zone J.*, 8, 1013–1030, <https://doi.org/10.2136/vzj2008.0183>, 2009.
- 750 Lehning, M., Doorschot, J., and Bartelt, P.: A snowdrift index based on SNOWPACK model calculations, *Ann. Glaciol.*, 31, 382–386, <https://doi.org/10.3189/172756400781819770>, 2000.
- Li, L. and Pomeroy, J. W.: Estimates of Threshold Wind Speeds for Snow Transport Using Meteorological Data, *J. Appl. Meteorol.*, 36, 205–213, [https://doi.org/10.1175/1520-0450\(1997\)0362.0.CO;2](https://doi.org/10.1175/1520-0450(1997)0362.0.CO;2), 1997.
- Licciulli, C., Bohleber, P., Lier, J., Gagliardini, O., Hoelzle, M., and Eisen, O.: A full Stokes ice-flow model to assist the interpretation of millennial-scale ice cores at the high-Alpine drilling site Colle Gnifetti, Swiss/Italian Alps, *J. Glaciol.*, 66, 35–48, <https://doi.org/10.1017/jog.2019.82>, 2020.
- 755 Liston, G. E. and Elder, K.: A meteorological distribution system for high-resolution terrestrial modeling (MicroMet), *J. Hydrometeorol.*, 7, 217–234, <https://doi.org/10.1175/JHM486.1>, 2006.

- Liston, G. E., Haehnel, R. B., Sturm, M., Hiemstra, C. A., Berezovskaya, S., and Tabler, R. D.: Simulating complex snow distributions in windy environments using SnowTran-3D, *J. Glaciol.*, 53, 241–256, <https://doi.org/10.3189/172756507782202865>, 2007.
- Lundin, J. M., Stevens, C. M., Arthern, R., Buizert, C., Orsi, A., Ligtenberg, S. R., Simonsen, S. B., Cummings, E., Essery, R., Leahy, W., et al.: Firm Model Intercomparison Experiment (FirnMICE), *J. Glaciol.*, 63, 401–422, <https://doi.org/10.1017/jog.2016.114>, 2017.
- Luo, Y., Arnold, J., Liu, S., Wang, X., and Chen, X.: Inclusion of glacier processes for distributed hydrological modeling at basin scale with application to a watershed in Tianshan Mountains, northwest China, *J. Hydrol.*, 477, 72–85, <https://doi.org/10.1016/j.jhydrol.2012.11.005>, 2013.
- Lüthi, M. and Funk, M.: Dating ice cores from a high Alpine glacier with a flow model for cold firn, *Ann. Glaciol.*, 31, 69–79, <https://doi.org/10.3189/172756400781820381>, 2000.
- Maeno, N. and Arakawa, M.: Adhesion shear theory of ice friction at low sliding velocities, combined with ice sintering, *J. Appl. Phys.*, 95, 134–139, <https://doi.org/10.1063/1.1633654>, 2004.
- Mariani, I., Eichler, A., Jenk, T. M., Brönnimann, S., Auchmann, R., Leuenberger, M., and Schwikowski, M.: Temperature and precipitation signal in two Alpine ice cores over the period 1961–2001, *Clim. Past*, 10, 1093–1108, <https://doi.org/10.5194/cp-10-1093-2014>, 2014.
- Martorina, S., Olivero, A., Loglisci, N., Pelosini, R., and Paesano, G.: Capanna Margherita - The highest meteorological station in Europe. Is it possible to consider it as representative of synoptic weather?, in: International Conference on Alpine Meteorology and MAP-Meeting, Brig, Switzerland, 2003.
- Naz, B. S., Frans, C. D., Clarke, G., Burns, P. J., and Lettenmaier, D. P.: Modeling the effect of glacier recession on streamflow response using a coupled glacio–hydrological model, *Hydrol. Earth Syst. Sc.*, 18, 787–802, <https://doi.org/10.5194/hess-18-787-2014>, 2014.
- Pomeroy, J. and Male, D.: Steady-state suspension of snow, *J. Hydrol.*, 136, 275–301, [https://doi.org/10.1016/0022-1694\(92\)90015-N](https://doi.org/10.1016/0022-1694(92)90015-N), 1992.
- Pomeroy, J. W. and Gray, D. M.: Saltation of snow, *Water Resour. Res.*, 26, 1583–1594, <https://doi.org/10.1029/WR026i007p01583>, 1990.
- Pomeroy, J. W., Gray, D. M., and Landine, P. G.: The Prairie Blowing Snow Model: characteristics, validation, operation, *J. Hydrol.*, 144, 165–192, [https://doi.org/10.1016/0022-1694\(93\)90171-5](https://doi.org/10.1016/0022-1694(93)90171-5), 1993.
- Pomeroy, J. W., Marsh, P., and Gray, D. M.: Application of a distributed blowing snow model to the Arctic, *Hydrol. Process.*, 11, 1451–1464, [https://doi.org/doi:10.1002/\(SICI\)1099-1085\(199709\)11:113.0.CO;2-Q](https://doi.org/doi:10.1002/(SICI)1099-1085(199709)11:113.0.CO;2-Q), 1997.
- Roe, G. H.: Orographic precipitation, *Annu. Rev. Earth Pl. Sc.*, 33, 645–671, <https://doi.org/10.1146/annurev.earth.33.092203.122541>, 2005.
- Schöner, W., Auer, I., Böhm, R., Keck, L., and Wagenbach, D.: Spatial representativity of air-temperature information from instrumental and ice-core-based isotope records in the European Alps, *Ann. Glaciol.*, 35, 157–161, <https://doi.org/10.3189/172756402781816717>, 2002.
- Seibert, J., Vis, M. J. P., Kohn, I., Weiler, M., and Stahl, K.: Technical note: Representing glacier geometry changes in a semi-distributed hydrological model, *Hydrol. Earth Syst. Sc.*, 22, 2211–2224, <https://doi.org/10.5194/hess-22-2211-2018>, 2018.
- Sigl, M., Abram, N. J., Gabrieli, J., Jenk, T. M., Osmont, D., and Schwikowski, M.: Record of black carbon (rBC), bismuth, lead and others from 1741 to 2015 AD from Colle Gnifetti ice cores GC15 and GC03B (Swiss/Italian Alps), PANGAEA, <https://doi.org/10.1594/PANGAEA.894787>, in supplement to: Sigl, M et al. (2018): 19th century glacier retreat in the Alps preceded the emergence of industrial black carbon deposition on high-alpine glaciers. *Cryosphere*, 12, 3311–3331, <https://doi.org/10.5194/tc-12-3311-2018>, 2018.
- Smiraglia, C., Maggi, V., Novo, A., Rossi, G., and Johnston, P.: Preliminary results of two ice core drillings on Monte Rosa (Colle Gnifetti and Colle del Lys), Italian Alps, *Geogr. Fis. Din. Quat.*, 23, 165–172, 2000.

- Stevens, C. M., Verjans, V., Lundin, J., Kahle, E. C., Horlings, A. N., Horlings, B. I., and Waddington, E. D.: The Community Firn Model (CFM) v1. 0, *Geosci. Model Dev.*, 13, 4355–4377, <https://doi.org/10.5194/gmd-13-4355-2020>, 2020.
- Suter, S., Laternser, M., Haeberli, W., Frauenfelder, R., and Hoelzle, M.: Cold firn and ice of high-altitude glaciers in the Alps: measurements and distribution modelling, *J. Glaciol.*, 47, 85–96, <https://doi.org/10.3189/172756501781832566>, 2001.
- 800 Vaughan, D. G., Comiso, J. C., Allison, I., Carrasco, J., Kaser, G., Kwok, R., Mote, P., Murray, T., Paul, F., Ren, J., Rignot, E., Solomina, O., Steffen, K., and Zhang, T.: Observations: Cryosphere, in: *Climate Change 2013: The Physical Science Basis. Contribution of Working Group I to the Fifth Assessment Report of the Intergovernmental Panel on Climate Change*, edited by Stocker, T. F., Qin, D., Plattner, G.-K., Tignor, M., Allen, S. K., Boschung, J., Nauels, A., Xia, Y., Bex, V., and Midgley, P. M., Cambridge University Press, Cambridge, United Kingdom and New York, NY, USA, 2013.
- 805 Vionnet, V., Guyomarc'h, G., Lafaysse, M., Naaim-Bouvet, F., Giraud, G., and Deliot, Y.: Operational implementation and evaluation of a blowing snow scheme for avalanche hazard forecasting, *Cold Reg. Sci. Technol.*, 147, 1–10, <https://doi.org/10.1016/j.coldregions.2017.12.006>, 2018.
- Wagenbach, D., Münnich, K., Schotterer, U., and Oeschger, H.: The anthropogenic impact on snow chemistry at Colle Gnifetti, Swiss Alps, *Ann. Glaciol.*, 10, 183–187, <https://doi.org/10.3189/S0260305500004407>, 1988.
- 810 Wagenbach, D., Bohleber, P., and Preunkert, S.: Cold, alpine ice bodies revisited: what may we learn from their impurity and isotope content?, *Geogr. Ann. A*, 94, 245–263, <https://doi.org/10.1111/j.1468-0459.2012.00461.x>, 2012.
- Wilkinson, D. S. and Ashby, M. F.: Pressure sintering by power law creep, *Acta Metall. Mater.*, 23, 1277–1285, [https://doi.org/10.1016/0001-6160\(75\)90136-4](https://doi.org/10.1016/0001-6160(75)90136-4), 1975.
- Wortmann, M., Bolch, T., Su, B., and Krysanova, V.: An efficient representation of glacier dynamics in a semi-distributed hydrological model
815 to bridge glacier and river catchment scales, *J. Hydrol.*, 573, 136–152, <https://doi.org/10.1016/j.jhydrol.2019.03.006>, 2019.